AFRL-AFOSR-VA-TR-2022-0011

AlGaN and AlGaN-based quantum wells: towards high-power high-frequency electronics

Sensale-Rodriguez, Berardi
UNIVERSITY OF UTAH SALT LAKE CITY
201 PRESIDENTS CIR RM 408
SALT LAKE CITY, UT,
US

10/26/2021
Final Technical Report

DISTRIBUTION A: Distribution approved for public release.

Air Force Research Laboratory
Air Force Office of Scientific Research
Arlington, Virginia 22203
Air Force Materiel Command

REPORT DOCUMENTATION PAGE			*Form Approved* *OMB No. 0704-0188*

The public reporting burden for this collection of information is estimated to average 1 hour per response, including the time for reviewing instructions, searching existing data sources, gathering and maintaining the data needed, and completing and reviewing the collection of information. Send comments regarding this burden estimate or any other aspect of this collection of information, including suggestions for reducing the burden, to Department of Defense, Washington Headquarters Services, Directorate for Information Operations and Reports (0704-0188), 1215 Jefferson Davis Highway, Suite 1204, Arlington, VA 22202-4302. Respondents should be aware that notwithstanding any other provision of law, no person shall be subject to any penalty for failing to comply with a collection of information if it does not display a currently valid OMB control number.
PLEASE DO NOT RETURN YOUR FORM TO THE ABOVE ADDRESS.

1. REPORT DATE *(DD-MM-YYYY)*	**2. REPORT TYPE**	**3. DATES COVERED** *(From - To)*
26-10-2021	Final	01 Aug 2018 - 31 Jul 2021

4. TITLE AND SUBTITLE
AlGaN and AlGaN-based quantum wells: towards high-power high-frequency electronics

5a. CONTRACT NUMBER

5b. GRANT NUMBER
FA9550-18-1-0332

5c. PROGRAM ELEMENT NUMBER
61102F

6. AUTHOR(S)
Berardi Sensale-Rodriguez

5d. PROJECT NUMBER

5e. TASK NUMBER

5f. WORK UNIT NUMBER

7. PERFORMING ORGANIZATION NAME(S) AND ADDRESS(ES)
UNIVERSITY OF UTAH SALT LAKE CITY
201 PRESIDENTS CIR RM 408
SALT LAKE CITY, UT
US

8. PERFORMING ORGANIZATION REPORT NUMBER

9. SPONSORING/MONITORING AGENCY NAME(S) AND ADDRESS(ES)
AF Office of Scientific Research
875 N. Randolph St. Room 3112
Arlington, VA 22203

10. SPONSOR/MONITOR'S ACRONYM(S)
AFRL/AFOSR RTA1

11. SPONSOR/MONITOR'S REPORT NUMBER(S)
AFRL-AFOSR-VA-TR-2022-0011

12. DISTRIBUTION/AVAILABILITY STATEMENT
A Distribution Unlimited: PB Public Release

13. SUPPLEMENTARY NOTES

14. ABSTRACT
Terahertz spectroscopy is an important tool for non-contact, non-destructive characterization of materials. From the transmission and reflection properties of samples through THz time domain and continuous wave spectroscopy it is possible to extract the dielectric properties of materials samples as well as the nanoscale transport properties of these. We have demonstrated this previously in complex oxides [1-2]. During this project, as research objective, we focused on the THz characterization of III-Nitrides through THz spectroscopy as well as explored the potentials of these materials for terahertz applications. We also developed new techniques and approaches towards materials characterization, which we employed not only in III-Nitrides, but also in other wide bandgap semiconductors.
B. Details of accomplishments
1- THz spectroscopy for anisotropic permittivit

15. SUBJECT TERMS

16. SECURITY CLASSIFICATION OF:			**17. LIMITATION OF ABSTRACT**	**18. NUMBER OF PAGES**	**19a. NAME OF RESPONSIBLE PERSON**
a. REPORT	**b. ABSTRACT**	**c. THIS PAGE**			KENNETH GORETTA
U	U	U	UU	32	**19b. TELEPHONE NUMBER** *(Include area code)* 426-7349

Standard Form 298 (Rev.8/98)
Prescribed by ANSI Std. Z39.18

AFOSR FINAL REPORT

Principal Investigator:

Dr. Berardi Sensale-Rodriguez

Associate Professor

Department of Electrical and Computer Engineering

The University of Utah

Salt Lake City, UT 84112

berardi.sensale@utah.edu

Project Title:

AlGaN and AlGaN-based QWs: towards high-power high-frequency electronics

Grant Number:

FA9550-18-1-0332

Period of Performance: August 2018 to August 2021

Report Date: October 25, 2021

DISTRIBUTION A: Distribution approved for public release.

Accomplishments

A. Research objectives

Terahertz spectroscopy is an important tool for non-contact, non-destructive characterization of materials. From the transmission and reflection properties of samples through THz time domain and continuous wave spectroscopy it is possible to extract the dielectric properties of materials samples as well as the nanoscale transport properties of these. We have demonstrated this previously in complex oxides [1-2]. During this project, as research objective, we focused on the THz characterization of III-Nitrides through THz spectroscopy as well as explored the potentials of these materials for terahertz applications. We also developed new techniques and approaches towards materials characterization, which we employed not only in III-Nitrides, but also in other wide bandgap semiconductors.

B. Details of accomplishments

1- **THz spectroscopy for anisotropic permittivity extraction**: demonstrate this technique for anisotropic permittivity extraction in an example highly anisotropic UWBG material. Was able to extract experimentally the full quasi-static permittivity tensor, which in such case is relevant and critical for device design and simulation.

2- **Boosting the sensitivity of terahertz spectroscopy for conductive layers**: THz spectroscopy can provide valuable information regarding the charge transport properties in semiconductors. But its application for the characterization of low-conductive two-dimensional layers, i.e., $\sigma s << 1$ mS, is limited due to the low sensitivity of direct transmission measurements to such small sheet conductivity levels. Harnessing the extraordinary optical transmission through gratings consisting of metallic stripes we demonstrated that is possible to characterize such low-conductive layers. We analyzed the geometric tradeoffs in these structures and provide physical insights, ultimately leading to general design guidelines for experiments enabling non-contact, non-destructive, highly sensitive characterization of such layers.

3- **Boosting the sensitivity of terahertz spectroscopy for out-of-plane permittivity extraction**: We demonstrated refractive index characterization of several semiconductor substrates with parallel metallic gratings through frequency-domain polarized terahertz transmission measurements. The metallic gratings consist of parallel gold strips and are easy to fabricate. Utilizing numerical simulations, the isotropic and anisotropic refractive indices were obtained by fitting the terahertz transmission spectrum of each sample. It is in particular noticed that in gratings with narrow gaps, it is possible to extract the out-of-plane component of refractive index with negligible uncertainty. This is demonstrated in a series of semiconductors enabling a simple approach for measuring refractive indices in the terahertz spectral range, which is particularly sensitive to out-of-plane index.

4- **Terahertz Metamaterial Modulators Based on Wide-Bandgap Semiconductor Lateral Schottky Diodes: unique potentials of AlGaN/GaN**. Efficient high-speed modulation and demodulation techniques are necessary for the development of future terahertz communication systems. However, the speed of state-of-the-art terahertz modulators is limited to MHz-GHz. In our work we demonstrate that lateral Schottky diodes in AlGaN/GaN can enable simultaneous high-speed modulation (>100GHz), large modulation depth (>10dB), and low-loss (<1dB) in a metamaterial configuration. These devices can therefore unlock the potentials of the terahertz band for future 6G wireless communications.

DISTRIBUTION A: Distribution approved for public release.

C. Dissemination of results to the communities of interest

Results were disseminated through journal publications and conference presentations. In addition to journal papers already published, we have several papers submitted or in preparation.

Journal papers:

- W. Jia *et al*, "Terahertz characterization of the effect of strain on the conductivity of AlGaN/GaN 2DEGs", in preparation. (FA9550-18-1-0332 primary sponsor)
- W. Jia and B. Sensale-Rodriguez, "Terahertz Metamaterial Modulators Based on Wide-Bandgap Semiconductor Lateral Schottky Diodes", submitted. (FA9550-18-1-0332 primary sponsor)
- W. Jia, P. Gopalan, A. Bhattacharyya, S. Krishnamoorthy, and B. Sensale-Rodriguez, "Anisotropic refractive index characterization through terahertz spectroscopy enabled by metal-gratings", submitted. (FA9550-18-1-0332 primary sponsor)
- P. Gopalan, Y. Wang, and B. Sensale-Rodriguez, "Terahertz characterization of two-dimensional low-conductive layers enabled by metal gratings", *Scientific Reports*, 2021. (FA9550-18-1-0332 primary sponsor)
- Banerji, S., Shi, Y., Su, V.S.E., Ghosh, U., Cooke, J., Kong, Y.L., Liu, L. and Sensale-Rodriguez, B., 2021. Inverse Designed THz Spectral Splitters. IEEE Microwave and Wireless Components Letters, 31(5), pp.425-428. (FA9550-18-1-0332 secondary sponsor)
- P. Gopalan *et al*, "The anisotropic quasi-static permittivity of single-crystal β-Ga2O3 measured by terahertz spectroscopy", *Applied Physics Letters*, 2020. (FA9550-18-1-0332 secondary support)
- S. Banerji, J. Cooke, and B. Sensale-Rodriguez, "Impact of fabrication errors and refractive index on multilevel diffractive lens performance". *Scientific Reports*, 2020. (FA9550-18-1-0332 secondary support)
- H. Condori *et al*, "Comparison of unit cell coupling for grating-gate and high electron mobility transistor array THz resonant absorbers", *Journal of Applied Physics,* 2018. As part of a collaboration with Prof. Xing's group (Cornell).

Conference presentations:

- B. Sensale-Rodriguez, Ultra-high-speed THz Modulation Based on Lateral Schottky Diodes in UWBG Semiconductors. Lester Eastman Conference on High Performance Devices, 2021.
- B. Sensale-Rodriguez, THz characterization and applications of wide bandgap materials : III-Nitrides and gallium oxide. RJUSE 2021.
- P. Gopalan, THz characterization of low-conductive sheet-charges with metallic gratings. 46th International Conference on Infrared, Millimeter and Terahertz Waves (IRMMW-THz) 2021
- P. Gopalan, Anisotropic Terahertz Permittivity of β-Ga2O3. In: IRMMWTHz 2020, Buffalo, NY. 2020.
- P. Gopalan, Anisotropic Terahertz Permittivity of β-Ga2O3. In: Electronic Materials Conference (EMC) 2020.

DISTRIBUTION A: Distribution approved for public release.

Significant awards:

- Hugo Condori, who was involved in this project during the fall semester of 2018, received the outstanding PhD dissertation award from the ECE department, University of Utah.
- Prashanth Gopalan, who was continuously supported by this project during its whole duration, was awarded the NIST award at the Electronic Materials Conference (EMC) 2020.

Impacts

D. Development of the principal discipline(s) of the project

The impact of this project is two-fold. From one side, we developed and demonstrated techniques that can enable very sensitive characterization of transport and dielectric properties in semiconductors. These techniques are non-contact and were applied to technologically relevant situations. One of such is the case of two-dimensional charge layers in III-Nitride quantum wells of low conductivity, e.g. a hole layer in AlGaN/GaN, another example is for the determination of effect of strain on the conductivity of transistors in such materials. These techniques were also demonstrated very sensitive for dielectric characterization. All this was possible through the use of metamaterials.

From the other side, an important impact of this project will be the finding that Schottky diode arrays in AlGaN/GaN could provide for a performance, as modulators, that is superior than that in any other semiconductor system. These could enable high-speed terahertz modulators unlocking high-speed communications in this frequency band. This is essential for the future of wireless communication systems.

Therefore, the impact of this project spans basic and applied research, materials, devices, as well as potentially systems and technologies. It also has an important impact in metrology, in particular non-contact very sensitive metrology of semiconductors.

E. Impact on the development of human resources

This project contributed strongly to the formation of human resources. The following students and projects were financially supported and performed research as part of this project.

- Prashanth Gopalan. PhD student, primary support, graduated
- Wei Jia. PhD student, secondary support.
- Jacqueline Cooke. PhD student, secondary support.
- Leila Ghadbeigi. Postdoc, partial support.
- Yu Kee Ooi. Postdoc, partial support.

F. Impact on physical, institutional, and information resources that form infrastructure

During this project, an important task that we carried out, was to setup measurement infrastructure. For the terahertz characterization of carrier transport of samples provided by partners (AFRL, Cornell and Ohio State), we require cryogenic measurements. For this purpose, we purchased and set up an optical cryostat to our THz spectroscopy setup. The cryostat is portable and can be integrated with our continuous wave as well as our time domain setups. Depicted below is a picture of the cryostat integrated with the continuous wave setup. In this case the cryostat is placed in the path of the incident beam, terahertz light is focused employing four parabolic mirrors, going

DISTRIBUTION A: Distribution approved for public release.

through the optical windows and the sample holder (located at the focus) inside the cryostat chamber.

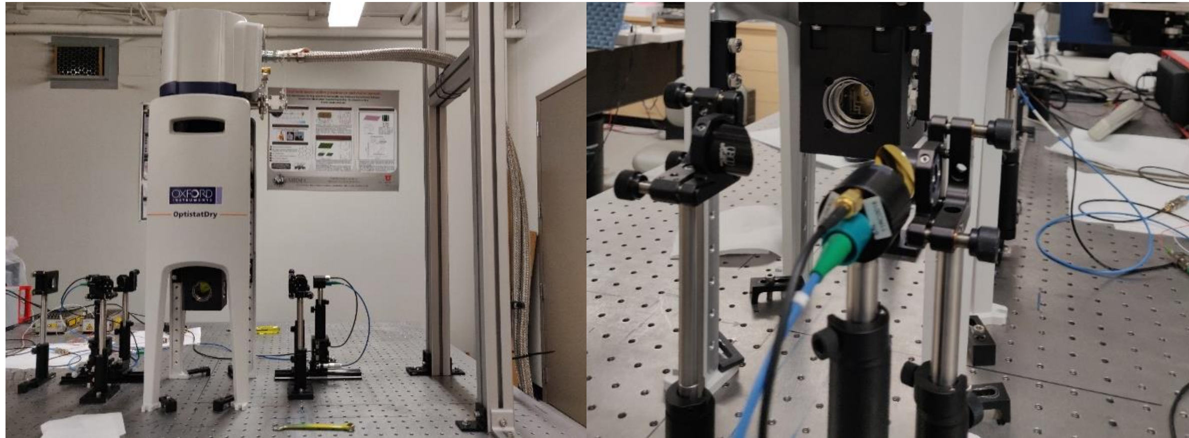

Image of the optical cryostat integrated in the CW THz setup. THz light is focused in a four-mirror configuration into a sample placed in the sample holder.

An important aspect of the project was also to investigate a sensitive measurement to sample anisotropy through focusing light of different polarizations and measure the transmission for p and s polarization (at same physical point) so to characterize flexible GaN samples. These samples are placed as depicted in the figure below in a sample holder which enables us to arbitrary harness amount of strain. Through performing this differential measurement, we are able to extract $\Delta\sigma$, the difference in conductivity, between the directions in which strain is / is not applied.

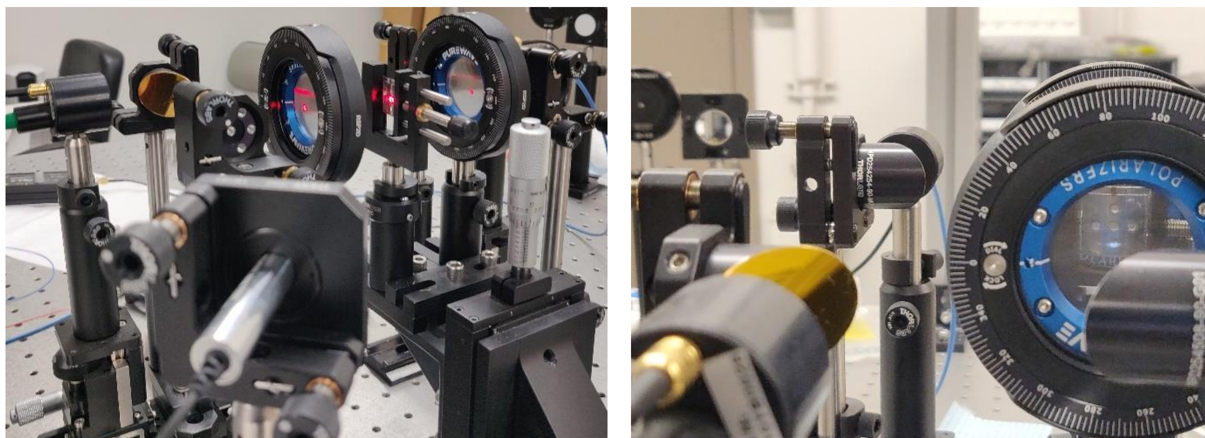

Optical setup in which strained samples are currently being characterized.

G. Impact on society beyond science and technology

The impact on society, beyond science and technology of this project is through the application that the materials studied in this project enable, such as more efficient power electronics, which could enhance the performance of systems and be more power efficient. Another example is through communication devices that could make our society more connected.

DISTRIBUTION A: Distribution approved for public release.

Changes

H. Changes in approach

The work in this project was heavily impacted by the COVID pandemic as well as infrastructure problems, e.g., breaking of optical cryostat and substantial delay in obtaining a new one, and lately a severe flood on campus. Experimental research was restricted over a substantial part of this project due to campus restrictions. As a result, we had to shift some work from experimental to theoretical/simulation research.

I. Problems and delays

As mentioned in the previous point, external causes affected the work in this project. However, we are currently finishing experimental work that we started that was caught midway because of these problems. We are pushing towards finishing this work. It is to mention that one manuscript is advanced in preparation (about characterization under strain), and we expect to finish a second one about low temperature characterization. These publications will obviously acknowledge support from this project.

Technical updates

J. Introduction

Background on III-Nitride characterization

As a first investigation on THz spectroscopy of III-Nitrides, which was used as preliminary data in this project, we investigated the nanoscale transport dynamics of carriers in strained AlN/GaN/AlN quantum wells (see **Fig. 1**): an electron-hole bilayer charge system with a large difference in transport properties between charge layers [3]. Often, electrical characterization of these complex electron-hole bilayer systems is performed via Hall-effect measurements. While conventional Hall-effect measurements provide a weighted average of the electron-hole bilayer system mobility and charge concentration, a more careful transport analysis is required to identify the individual effects of each type of carrier.

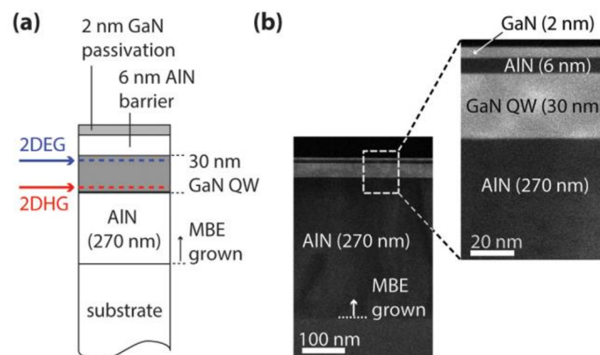

Figure 1. *(a) Schematic cross section of the analyzed QWs. (b) TEM image of a representative QW under study.*

In our study, we are able to decouple the electron and hole transport properties in this QW system system by means of non-contact THz spectroscopy. Since the charge layers (2DEG and 2DHG) exhibit distinct spectral signatures at terahertz frequencies, a combination of terahertz and far-infrared spectroscopy enables us to extract individual contributions to the total conductivity as well

DISTRIBUTION A: Distribution approved for public release.

as effective scattering rates for charge-carriers in each layer. This was performed by fitting the measured transmission spectra through the sample to an analytical model assuming an overall sheet conductivity of the form:

$$\sigma_b(\omega) = \frac{\sigma_e^0}{1 + j\omega\tau_e} + \frac{\sigma_h^0}{1 + j\omega\tau_h}$$

Where σ_b represents the overall sheet conductivity of the bilayer system, σ_e^0 and σ_h^0 are the quasi-static conductivities, and τ_e and τ_h the momentum relaxation times for electrons (e) and holes (h), respectively. Depicted in **Fig. 2** is a representative transmission spectrum together with its fit.

Furthermore, by comparing direct-current and THz-extracted conductivity levels, we are able to determine the extent to which structural defects affect charge transport. Although terahertz spectroscopy enables us to directly extract the conductivity and relaxation times associated with charge carriers, it is also possible to indirectly extract other parameters, such as charge density and mobility, by assuming an appropriate effective mass. By assuming an electron effective mass of $m_e = 0.2m_0$, electron drift mobilities ranging from ~800 to 1,200 cm^2/Vs are extracted across a set of analyzed samples. A comparison of these mobility levels with those extracted from Hall measurements, shows a much larger electron drift mobility extracted from THz measurements than the Hall mobility measured across all samples (μ_{Hall} ranging from ~100 to 400 cm^2/Vs). These results evidence that (i) a non-unity Hall-factor and (ii) the considerable contribution of holes to the overall conductivity led to a lower apparent mobility in Hall-effect measurements. Overall, this work demonstrates that terahertz spectroscopy is a suitable technique for studying bilayer charge systems with large differences in transport properties between layers such as quantum wells in III-nitride semiconductors.

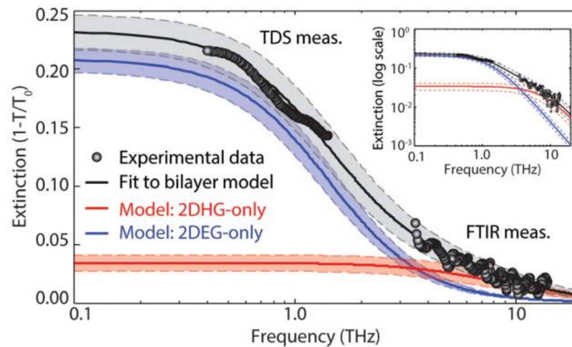

Figure 2. Representative extinction spectra over an extended frequency range. The data from 0.4 to 1.4 THz were obtained via THz-TDS, while the data from 3 to 14 THz were obtained via FTIR spectroscopy. The continuous black line corresponds to the best fit of the measured data to the analytical model. For reference, modeled spectral signatures corresponding to a 2DEG-only (blue) and a 2DHG-only (red) exhibiting zero-frequency conductivities and relaxation times consistent with those experimentally extracted for this sample are also shown in the plot. The colored shaded regions located between dashed traces represent uncertainty margins at the 95% confidence level. The inset depicts the same plot on a log-log scale, showing in more detail the fit of the high frequency data to the model.

DISTRIBUTION A: Distribution approved for public release.

THz spectroscopy for anisotropic permittivity extraction

Terahertz spectroscopy can resolve for anisotropic transport and dielectric properties in materials. As such it can enable extraction of quasi-static anisotropic permittivity parameters. As an example, we analyzed electrically insulating beta gallium oxide (β-Ga_2O_3), which is a highly anisotropic wide bandgap semiconductor [4]. Depicted in **Fig. 3** is a sketch of a unit cell together with crystallographic orientation definitions. Polarization-resolved frequency domain spectroscopy in the spectral range from 200 GHz to 1 THz was carried out on bulk crystals along different orientations. From these measurements, principal directions for permittivity were determined along crystallographic axes *c* and *b* and reciprocal lattice direction a^*. This is very important, since in principle the principal directions for permittivity do not necessarily match crystallographic axes.

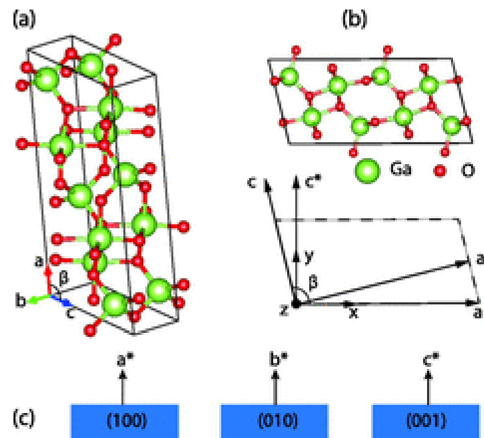

Figure 3. (a) The unit cell of β-Ga2O3 with monoclinic angle β and crystal unit axes a, b, and c. (b) Monoclinic plane a–c viewed along axis b (b points into the plane). Definition of the laboratory Cartesian coordinate system (x, y, z) and crystal unit axes (a, b, c). Reciprocal lattice vector c⋆ parallel to axis y, a parallel to axis x, and b parallel to axis z (not drawn to scale). Principal plane Miller indices for surfaces of samples investigated here are shown in (c), with surface normal reciprocal lattice vectors. Note that b⋆||b. The relationship between the laboratory coordinate system (x, y, z) and the monoclinic system (a, b, c) shown in (b) is valid for all surface orientations shown in (c).

Transmission measurements were performed employing continuous wave THz spectroscopy as well as ellipsometry in several samples (differently oriented bulk crystals). An example is provided in **Fig. 4**. The sample orientation was rotated with respect to the polarization of the incident terahertz beam and the corresponding transmission was measured at several angles in the a-c plane. Given the insulating nature of the sample (Fe-doped substrate), we expect to observe single-mode Fabry-Pérot (FP) oscillations when the incident E-field is along a major polarizability axis with the transmission levels at the FP maxima approaching near unity. Our measurement of polarization-resolved transmission at different angles in the a-c plane indicate that the principal axes are close to a^* and *c*-directions in the (010). **Fig. 4(a)** and **(b)** show the transmitted E-field amplitude when the directions a^* and c are aligned with the incident polarization, respectively. Fig. 3(c) depicts the transmission of the (001) surface with the b axis parallel to the incident polarization. The index of refraction values extracted from these particular analyses are $n_{a*} = 3.16 \pm 0.09$, $n_c = 3.51 \pm 0.10$ and $n_b = 3.18 \pm 0.035$. No frequency dispersion was observed as evidenced by a constant free spectral range over the measured spectral range.

DISTRIBUTION A: Distribution approved for public release.

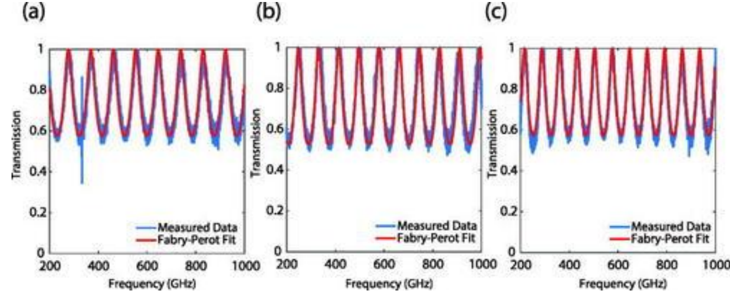

Figure 4. *Experimental (blue) and best-match calculated (red) polarized transmission measured for electric field directions parallel to (a) a* -axis [(010) β-Ga_2O_3], (b) c-axis [(010) β-Ga_2O_3], and (c) b-axis [(001) β-Ga_2O_3]. The variation in the Fabry–Pérot fringes between spectra shown in (a) and (b) reveals the strong anisotropy between the permittivities for directions a⋆ and c.*

K. Overview of main accomplishments

Terahertz characterization of two-dimensional low-conductive layers enabled by metal gratings

Although terahertz spectroscopy can provide valuable information about the charge transport properties in semiconductors, its application to the characterization of low-conductive two-dimensional layers, i.e., $\sigma_s << 1$ mS, remains elusive. This is owed to the low sensitivity of direct transmission measurements to such small conductivity levels. In our work, we discuss metamaterial approaches for the characterization of such low-conductive two-dimensional layers. We analyzed the geometric tradeoffs in these structures and provide physical insight, ultimately leading to general design guidelines for experiments enabling non-contact, non-destructive, highly sensitive characterization of such samples [5].

i. Motivation and background:

It is worth noting that at terahertz frequencies, following a Debye model, the charge carrier conductivity is effectively determined over characteristic length scales on the order of nm's. The sheet conductivity extracted from terahertz measurements is, from this perspective, a spatially averaged nanoscale conductivity and is thus less affected by microscale effects that usually affect direct current (DC) transport measurements wherein transport is typically probed over three-orders of magnitude larger length scales (µm). These include extended effects such as those arising from point defects or dislocations introduced during growth in epitaxial layers, or grain boundaries that are usually present in two-dimensional films. As a result, charge transport characterization using terahertz spectroscopy can provide a more relevant estimate of the intrinsic electrical properties of such conductive layers. Furthermore, the terahertz-extracted sheet conductivity is more relevant for use in optoelectronic or nano-electronic devices, where the relevant dimensions for charge transport, as dictated, for instance, by the gate-length in field-effect transistors, are also on the order of nanometers. Besides, the frequency dependence of conductivity can also provide valuable information on the physical nature of charge transport as well as dominating scattering mechanisms.

However, the extraction of the terahertz conductivity of such conductive layers from direct transmission measurements is fundamentally limited to a narrow range of conductivity values. These are dictated by the sensitivity of transmission itself to conductivity. For illustrative purposes, let us assume that we have a two-dimensional conductive layer suspended in free space. This layer

DISTRIBUTION A: Distribution approved for public release.

is impinged by a normally incident terahertz beam, as illustrated in **Fig. 5a**. The conductivity of the layer (σ_s) is assumed to have no frequency dispersion over the analyzed frequency range. The transmittance, defined as the ratio between the transmitted powers in the absence (T_0) and presence (T) of the layer under test, is then given by:

$$\frac{T}{T_0} = \frac{4}{(2+Z_0\sigma_S)^2}.$$

Where $Z_0 \sim 377\ \Omega$ is the characteristic impedance of free space. Depicted in **Fig. 5b** is a plot of transmittance versus sheet conductivity (semi-log scale). It is observed that both at low conductivity levels (µS range) and high conductivity levels (S range), transmission approaches unity and zero, respectively; thus, such transmittance levels are challenging to discern practically. By taking the derivative of the previous equation, with respect to the logarithm of conductivity, we can estimate the associated transmission sensitivity to the sheet conductivity:

$$\frac{dT/T_0}{dLn(\sigma_S)} = \frac{-8Z_0\sigma_S}{(2+Z_0\sigma_S)^3}.$$

Figure 5b shows the calculated transmission sensitivity versus sheet conductivity. It is observed that as the conductivity approaches zero, the transmission sensitivity also approaches zero. This situation becomes effectively the case when $\sigma_s << 1/Z_0 \sim 2.65$ mS. From this perspective, it results extremely challenging to characterize conductive layers with conductivity levels on the order of µS, which is often the case in single layer TMDCs such as MoS_2, WSe_2, etc. as well as in conductive layers formed in heterostructures such as the two-dimensional hole gas (2DHG) formed at the interface of thin undoped Gallium Nitride (GaN) quantum wells (QWs). Therefore, to be able to characterize the transport properties of such low-conductive two-dimensional layers through terahertz spectroscopy, alternative approaches to direct transmission or reflection spectroscopy should be employed.

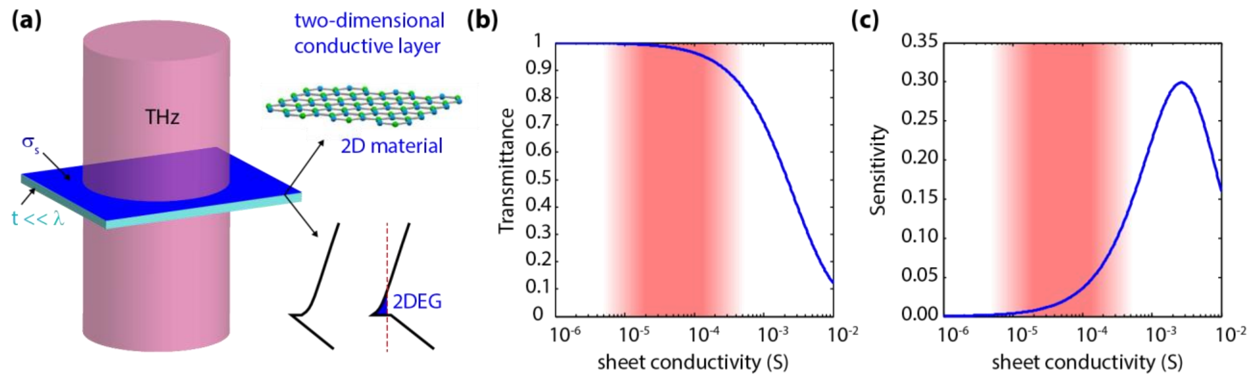

Figure 5. *Problem: how to characterize through THz spectroscopy a sample that is not conductive enough so to yield a discernible change in transmission /reflection?*

Recently, metamaterials have gained lots of attention for terahertz sensing applications. Some highly promising geometries consist of extraordinary optical transmission (EOT) structures, and metamaterials harnessing Fano and multipole resonances, among others. However, in contrast to most widely analyzed sensing applications, where typically the real part of permittivity is of interest, in low-conductive two-dimensional layer characterization, the imaginary part is what is relevant. Conceptually, considering the response of the metamaterial structures from an equivalent circuit perspective, this is manifested by the addition of an equivalent resistance when the layer under test is introduced. This is different from the typically analyzed case in refractive index

DISTRIBUTION A: Distribution approved for public release.

sensing, wherein capacitance is what is altered. From this perspective, although conceptually, these sensing problems are very similar, in many scenarios, the solution space can, in principle, significantly differ.

Furthermore, to guarantee that the measurements are non-destructive, the metasurface needs to be relatively far away spaced from the layer that is being probed. This can further compromise the application of several structures proposed for sensing like, e.g., small gap split-ring resonators. Furthermore, as will be later discussed in this study, the response of Babinet's complementary structures, e.g., a cross-slot metasurface being complementary to a cross array, can be more sensitive than that of the direct pattern. These particularities are essential to low-conductive layer characterization applications and should be considered and guide the design of highly sensitive metasurfaces.

Another important practical aspect is that many times is of interest to characterize anisotropic transport properties. This is the case, for instance, for Gallium Oxide (Ga_2O_3), an emerging semiconductor material, which is highly anisotropic. In this material, the extent to which crystal anisotropy and growth induced effects affect transport is a topic of current scientific debate. To uncouple the intrinsic and extrinsic properties of this material is therefore highly relevant, and terahertz spectroscopy can provide such answers not only in films, as recently reported, but also in two-dimensional electron gas (2DEG) charge layers. This is also for instance the case when investigating transport properties in samples under strain. Motivated by this, metasurfaces with an isotropic response might be preferred so to enable direct comparison of transport across different directions in a direct manner.

Through a systematic study of different proposed metasurface geometries, and thoroughly analyzing the tradeoffs in these, this work identifies several promising geometries and general design guidelines for low-conductive layer terahertz characterization.

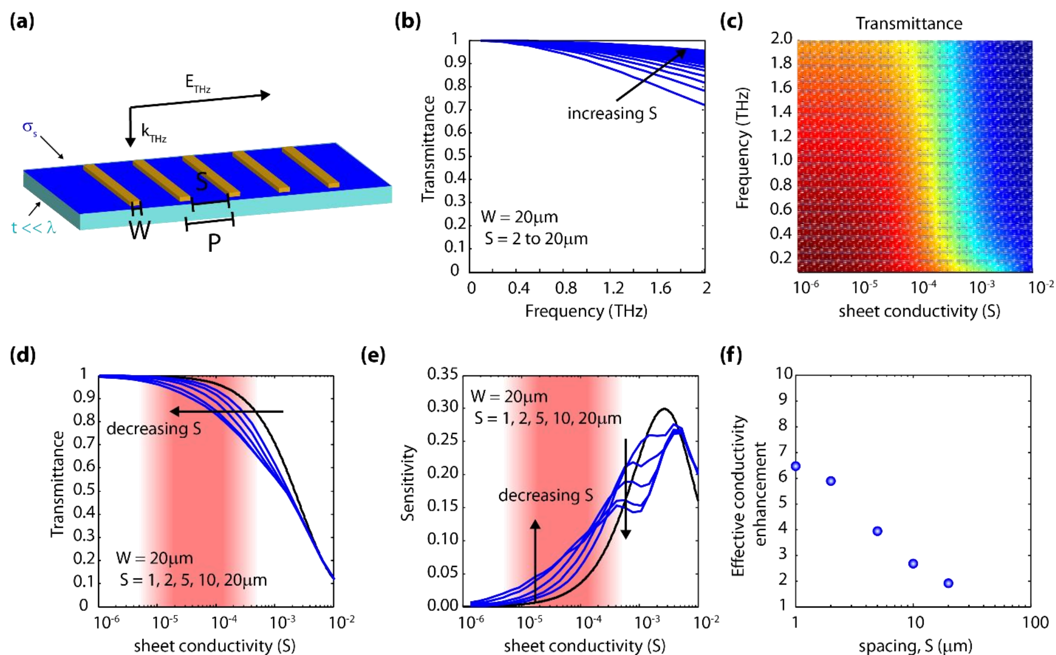

Figure 6. *Non-resonant gratings (P << λ) can provide some limited sensitivity improvement with typical optical lithography features (>1 μm).*

DISTRIBUTION A: Distribution approved for public release.

ii. Summary of key results and discussion

We first analyzed the response of a grating structure, as depicted in **Fig. 6a**. For this analysis, we varied the width (W) of the parallel metallic stripes as well as the spacing (S) between them. The response of this structure shows two different regimes, a resonant one when the period (P) is $P \gg \lambda$, and a non-resonant one, when $P \ll \lambda$. When $P \ll \lambda$, the transmission response of the grating follows that of a low pass filter. Therefore, a broadband region with high transmittance (passband) is observed, as illustrated in **Fig. 6b**.

The addition of the conductive layer alters the transmission levels in the passband. **Figure 6c** depicts the simulated transmittance spectra while varying conductivity (for S = 2 μm). By varying S, while keeping W constant, we generated a plot, **Fig. 6d**, with families of curves representing transmittance versus conductivity at the passband. It is observed that as the spacing, S, is decreased, the curves shift towards lower conductivity levels. This effect is further elaborated in **Fig. 6e**, which depicts the transmission sensitivity for different values of S. In the low conductivity regions, i.e., μS, the sensitivity is enhanced. Physically, this can be understood from the perspective of an effective conductivity enhancement (which directly follows the field enhancement). Shown in **Fig. 6f** is the extracted conductivity enhancement, defined as the ratio between the actual layer conductivity and the conductivity level that would provide an equivalent drop in transmission in the case where no metasurface is present. We observe that the smallest the spacing, the larger the enhancement. However, in order to push this region of high sensitivity to lower values, the dimension of the spacing needs to be reduced well below 1 μm. This is an issue from the fabrication perspective and limits the application of this approach.

In general, increasing the filling factor, defined as $f = W/P$, is critical, so to enhance the effective conductivity. For analyzing this effect, we performed simulations keeping S constant (S = 2 μm) and varying W. In this case, we observe that as W is increased, the transmission response shifts from a non-resonant regime to a resonant response, as shown in **Fig. 7a**. This is an effect well known from grating theory. To understand the effect of this phenomenon on the transmission spectra when incorporating a conductive layer, we performed simulations by varying W as well as σ. We observe in all cases that the transmittance amplitude at the resonance is altered when σ is varied. The position of the resonance does not significantly shift as σ is altered. However, this position does strongly shift with W. Depicted in **Fig. 7b** is the transmission spectra for a grating with W = 200 μm, the transmission is highly sensitive to the conductivity of a layer placed on its proximity. **Figure 7c** shows the extracted family of curves representing transmittance levels (at the resonance) versus layer conductivity for different values of W. It is observed that as the filling factor is increased (by increasing W), the transmittance characteristics shift towards lower conductivity levels. The curves in this case effectively shift to the region of interest. It is to note, as an example, that when W = 1000 μm and S = 2 μm, an exceptional, ~600X conductivity enhancement is observed at a sheet conductivity of ~50 μS as depicted in **Fig. 7d.**

At this end, we now discuss the effect of altering the spacing (d) between the metasurface and the conductive layer, as illustrated in **Fig. 7e**. Depicted in **Fig. 7f** is the simulated transmittance spectra for d = 0.1, 1, and 3 μm. It is observed, **Fig. 7g**, that the insertion of a few μm thick spacing alters the results by introducing a shift on the most sensitive region. This can be understood on basis of a smaller field enhancement as depicted in **Fig. 7h**. However, this region still remains in the μS range. From this perspective, as well as that of lithographic dimensions, grating structures consisting of large metal filling factors, $f > 0.99$, and moderate gaps, S ~ 2 – 5 μm, can be a good choice for low-conductive layer sensing applications. However, the response of these gratings is

DISTRIBUTION A: Distribution approved for public release.

strongly polarization-dependent, and therefore conductivity characterization can be performed only along a particular direction (i.e., along the direction perpendicular to the grating stripes).

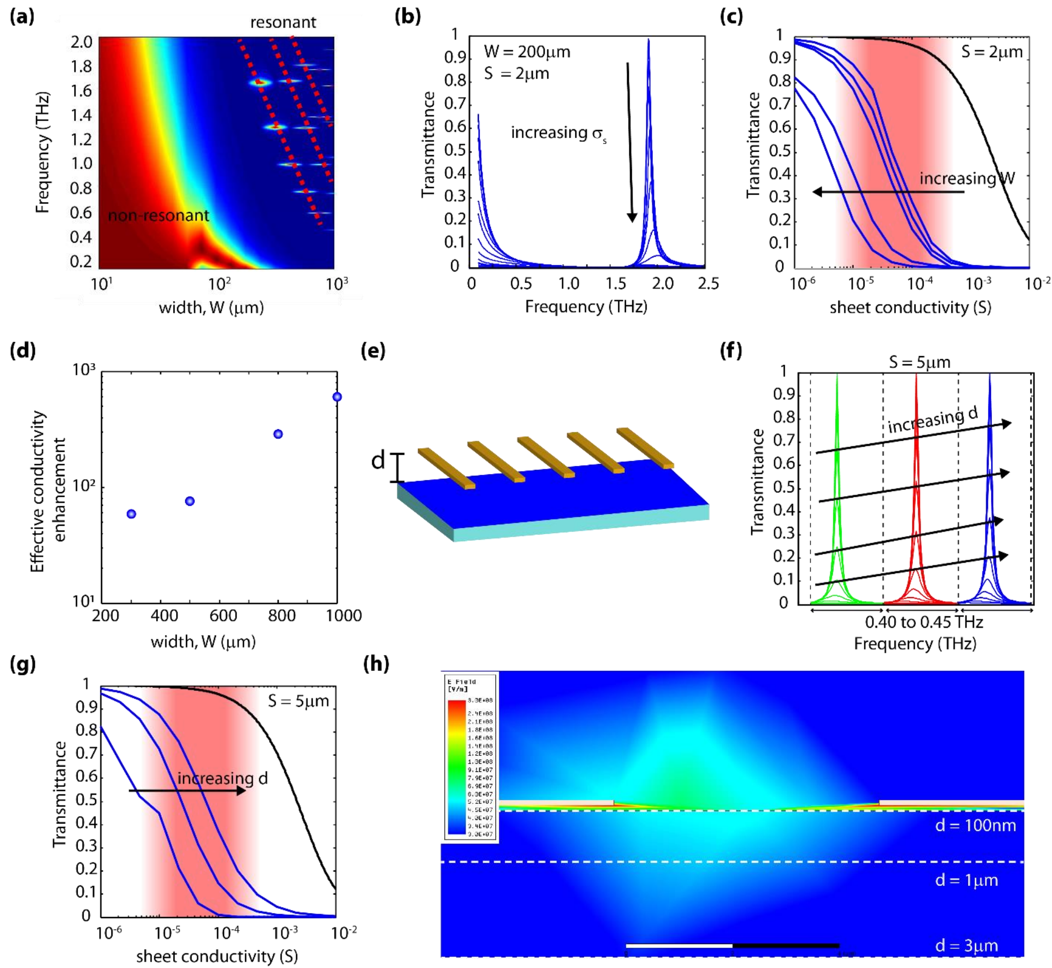

***Figure 7**. Resonant gratings can provide very strong field thus effective conductivity enhancements, therefore enabling very sensitive characterization of samples with μS level conductivities.*

In order to attain a polarization-independent response, we analyzed e.g., ring and ring-slot arrays. For illustrative purposes, we performed simulations for structures with a periodicity, P, of 550 μm, ring lateral dimension, W, 450 μm, and ring width, S, 2 μm. An illustration of the analyzed ring and ring-slot geometries is shown in **Fig. 8a**. The transmittance spectra for different sheet conductivity levels are depicted in **Figs. 8b**, for the ring, and **8d**, for the ring-slot, respectively. It is to note, as illustrated in **Figs. 8b** and **8d**, that although both structures exhibit resonances with a similar quality factor (the spectra are complimentary), the ring array shows a much smaller sensitivity to low layer conductivities when compared to its complementary structure. This can be understood from a smaller field enhancement (at resonance). Therefore, not only the quality factor but also the field enhancement is important when designing structures for low conductive layer sensing applications.

DISTRIBUTION A: Distribution approved for public release.

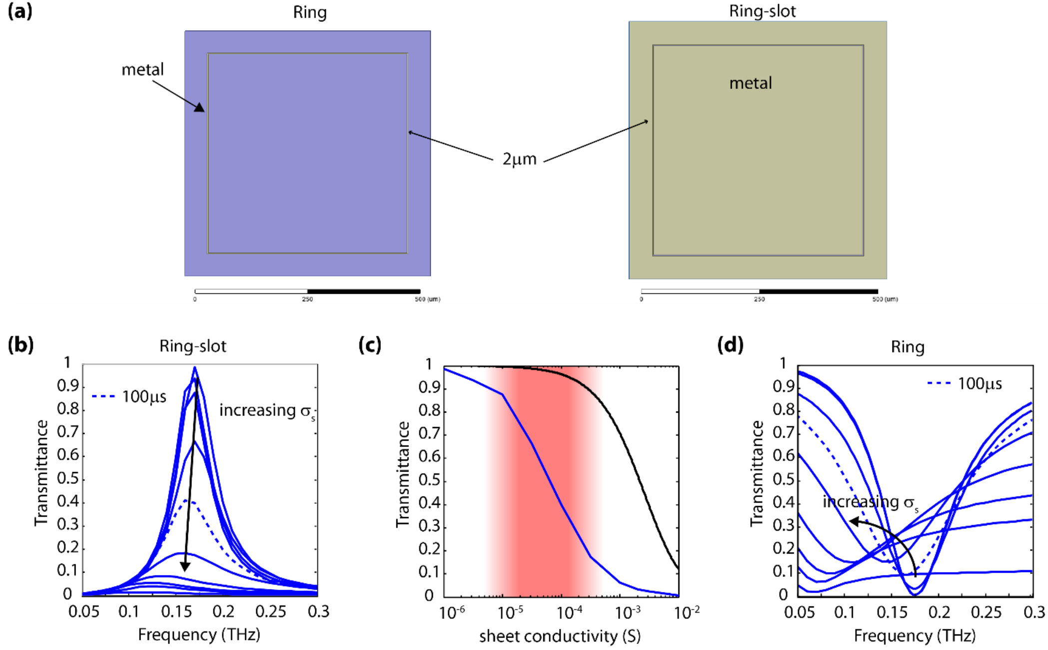

Figure 8. *Complementary structures, e.g., a ring-slot, can provide better performance than direct geometries. Through designing periodic structures with large period and small gaps relative to the period, it is possible to attain very sensitive transmission.*

iii. Example application: quantifying effect of strain on conductivity

Our goal was to analyze the effect of strain on the transport properties of 2DEGs in AlGaN/GaN HEMT structures. Analyzing the effect of strain on AlGaN/GaN HEMT structures on flexible substrates is a topic that has recently gotten substantial attention and where conflicting trends have been reported in the literature. This is an effect that can be measured, for instance, by laying out devices oriented differently with respect to the direction in which strain is applied. This is what is usually performed in reported experiments. However, these devices are independent devices thus conclusions can be difficult to be drawn given fabrication and growth inhomogeneities. Because of this, we explored non-contact polarization dependent THz spectroscopy as a way to characterize transport properties along different directions in the sample under strain.

To summarize the conflicting reports in the literature, it is to mention that Wang et al discussed that external strain changes the band bending at the AlGaN/GaN interface and can increase or decrease the charge density [6]. Mobility can be also affected by strain. Here, experimentally, through measuring the DC characteristics of three independent FETs laid out at different orientation with respect to strain 0^0, 45^0 and, 90^0, a substantial drop in mobility, around 40% was reported at 0.2% strain. It is to mention that this is accompanied by also a reduction in 2DEG charge density, in this case of around ~10%.

The effect of strain on effective mass has been discussed previously theoretically by Dreyer et al, but expected to be a relatively small effect (<5% variation) [7]. Biaxial stress can alter the effective mass of the carriers differently along different directions. But such a small variation might not be enough to produce large changes in mobility along different directions as reported by Wang.

DISTRIBUTION A: Distribution approved for public release.

AFRL has recently demonstrated flexible GaN transistors from heterostructures grown on BN [8]. In these samples, a small decrease in mobility but increase in charge density were observed. In this regard, the reduction in mobility observed in the 2DEG under strain (~5%) is counteracted by a slight increase in n_{2DEG} (~5%). The authors explain this increase with piezo and spontaneous polarization contributions in AlGaN and GaN. It is to mention that later work by the same group reported on an opposite trend for charge (on samples with low surface state densities); however, still a very small conductivity change is reported [9].

As part of our investigation, we studied samples grown by AFRL, which were transferred to PET substrates to enable transparency of the substrate at THz frequencies. We acknowledge the support of Michael Snure and Nicholas Glavin for providing these samples. In order to characterize these samples, following discussion with AFRL, we fabricated a mount wherein we can actively apply strain. Depicted in **Fig. 9a** are optical images of the sample holder, containing a sample, as well as the sample being characterized through Raman. Through this measurement, we were able to estimate the applied strain. It is observed that 1.5 turns of knob in the holder lead to ~0.11% strain (shift of peak from 568.4 to 569.0 cm^{-1}), three turns were found to lead to ~0.20% strain.

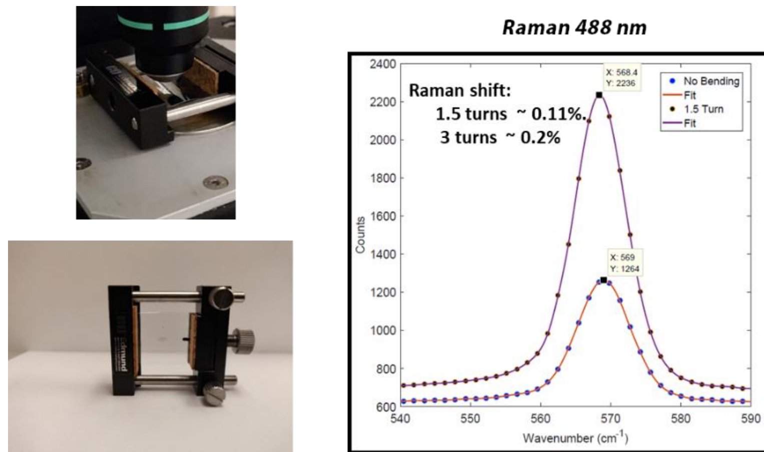

Figure 9. *Raman characterization. (a) optical image of sample holder and sample during Raman characterization (b) Raman spectra when applying strain to the sample.*

In order to study the effect of strain on the electrical conductivity of the sample, we directly measured the sample applying strain. For this purpose, polarization of a normally incident terahertz beam, which was focused in the samples, was set parallel to the direction of strain as illustrated in the insets in **Fig. 10**. We found that the measurement does not yield any discernible variations as strain was applied; large transmission levels (around 96%) are observed under no bending, 0.11%, and 0.20% strain.

The apparent conductivity levels, based on the transmission drop, where estimated to be very roughly ~0.6 mS. It is to mention that the sample under test is smaller than the size of our beam. Assuming a filling factor, through dividing the area of the sample over the size of the beam, we estimate the actual conductivity to be ~2X larger than what is extracted from the measurement (assuming a uniform conductivity over the beam area). Thus, we expect the actual sheet conductivity of the 2DEG to be ~1.2 mS thus consistent with our expectations from mobility and charge densities reported by AFRL in similar samples.

Because of the large uncertainty in the direct conductivity extraction from the transmission measurement, as transmission levels are between 0.9 and 1, we incorporated a metasurface in order

DISTRIBUTION A: Distribution approved for public release.

to enhance the sensitivity of transmission to conductivity following our previous discussion in [5]. For this purpose, following the general guideline summarized in **Fig. 8**, we chose a ring slot array so to provide for an electromagnetic response that is polarization independent.

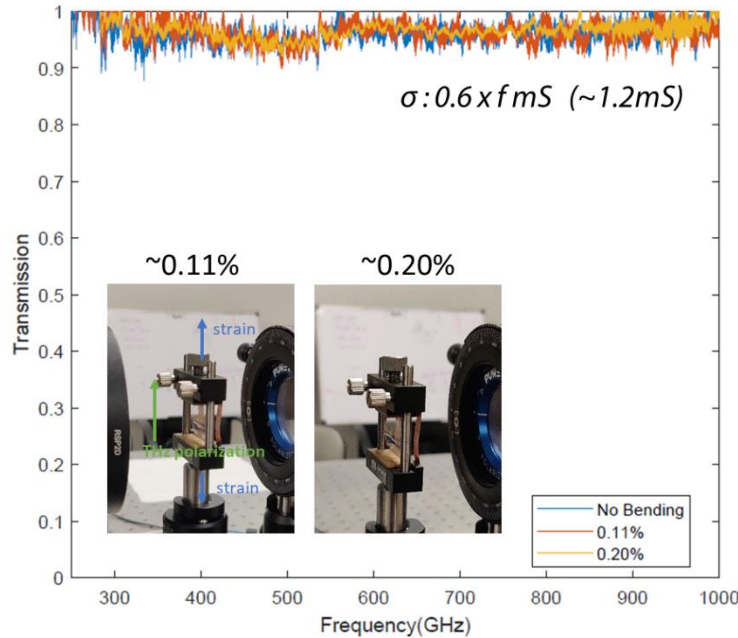

Figure 10. *THz characterization. Transmission vs. frequency for a sample non-bent, at 0.11% strain, and at 0.20% strain. The insets depict the sample under test. The polarization of the normally incident THz beam is set to be parallel to the direction in which strain is applied.*

The metallic ring structure was placed on top of the sample separated by a 2um thick perylene spacer. Perylene deposition, metal (Au) evaporation, and liftoff were carried out at the University of Utah nanofab. Depicted in **Fig. 11** are simulations of transmittance for difference conductivity levels in the sample (**Fig. 11a**), as well as the extracted peak transmittance vs. conductivity (**Fig. 11b**). When comparing the response of the 2DEG plus metasurface structure versus that of the 2DEG only, as shown in **Fig. 11**, we observe a strong enhancement of the sensitivity of the measurement to the 2DEG conductivity levels expected from the sample based on our results in **Fig. 10**. In **Fig. 11b**, the red curve represents transmission versus apparent conductivity for the direct measurement as depicted in **Fig. 10**. Our measurements for transmission lead in this case to levels close to unity (with average ~96% in the measured 0.25 - 1.0 THz frequency range). The yellow line in **Fig. 11b** depicts the uncertainty in this value. Through employing a metasurface we can reduce uncertainty and extract thus more accurate conductivity values; therefore, determine with more accuracy whether there are strain induced conductivity variations in the analyzed samples.

Shown in **Fig. 12a** is the measured response of a reference metasurface (metasurface fabricated on a bare PET substrate, i.e., without 2DEG) together with the simulation results for such a structure. A good agreement is observed between simulations and experimental results. The measured transmission spectra closely follows the simulated one previously with peak transmittance levels close to 80%. Differences arise from imperfections in metal, that is larger loss leading to

DISTRIBUTION A: Distribution approved for public release.

broadening of the peak and lower peak transmittance. Depicted in **Fig. 12b** is an optical image of the fabricated samples. The gap in the ring was set to 2 µm and the unit cell period is 150 µm.

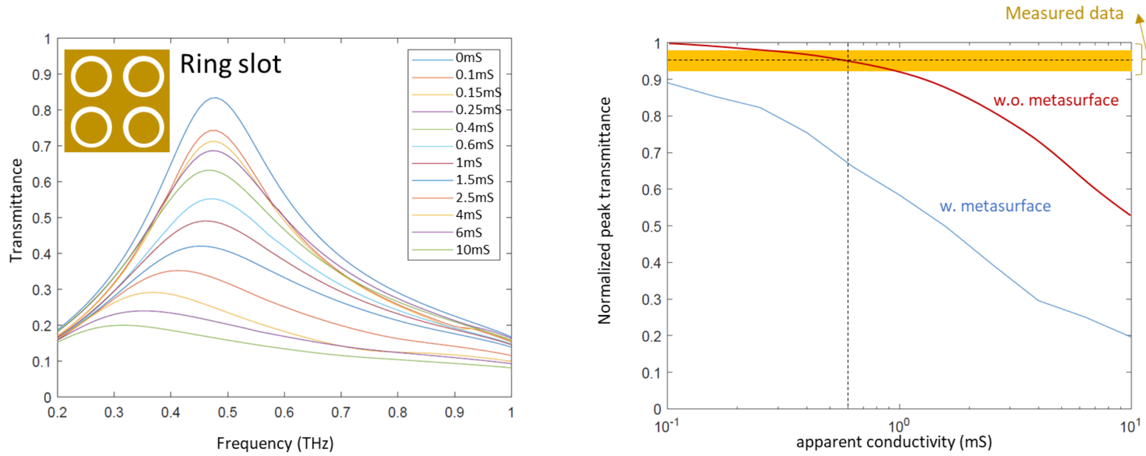

Figure 11. *THz simulations. (a) Transmission vs. frequency for a 2DEG plus ring slot metasurface structure. The different curves correspond to different 2DEG conductivity levels. (b)normalized peak transmittance versus apparent conductivity in the sample. A strong enhancement of the sensitivity of transmission (to the expected apparent conductivity levels for the samples under test) is predicted.*

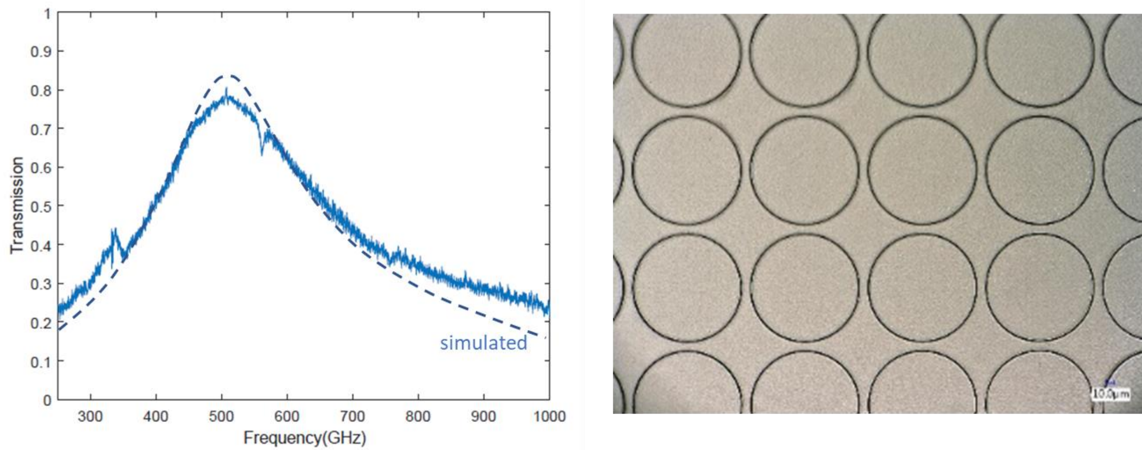

Figure 12. *(a) Measured and simulated transmission vs. frequency for a reference ring slot metasurface metasurface structure. (b) Optical image detail of the fabricated sample.*

Depicted in **Fig. 13** are the results (transmission spectra) for unbent, blue curves, as well as bent samples at 0.2% strain, red curves. **Figure 13a** shows transmission when the polarization is parallel to the direction in which strain is applied, whereas **Fig. 13b** shows transmission for polarization perpendicular to the direction in which strain is applied. When the polarization of the incident terahertz beam is perpendicular to the direction in which strain is applied, we observe no changes in the measured transmission spectra when bending, as expected. When the polarization is parallel, a slight apparent decrease in peak transmittance is observed. However, this decrease (corresponding to an apparent conductivity increase from 0.73 ± 0.09 mS to 0.81 ± 0.07 mS and

DISTRIBUTION A: Distribution approved for public release.

associated 2DEG conductivity from 1.46 ± 0.18 mS to 1.62 ± 0.14 mS), falls between the uncertainty margins of this measurement.

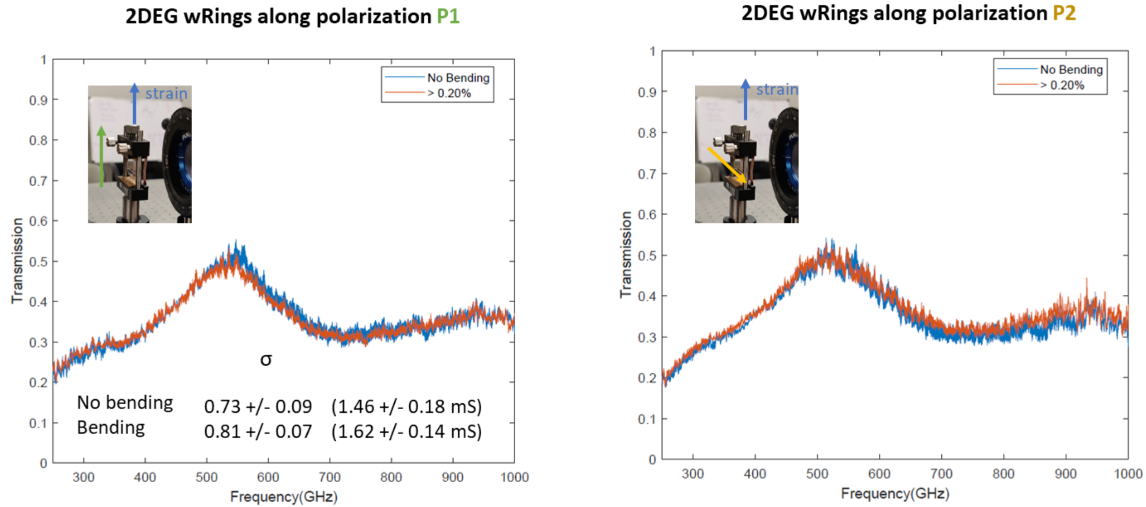

Figure 13. *Measured transmission spectra for incident terahertz beam polarization (a) parallel and (b) perpendicular to the direction in which strain is applied.*

Therefore, from the perspective that the variations in extracted conductivity levels fall in between error margins, we can conclude that if there is a variation in conductivity with strain, it is likely an increase (as strain is applied), and that this variation in any case is smaller than 10%. Therefore, the obtained results are consistent with those reported by AFRL from DC measurements in these AlGaN/GaN 2DEGs. Our results confirm that in these samples small or no conductivity variations take place as strain is applied. These results differ from observations by Wang et al where 40-50% variations in conductivity were reported in similar 2DEGs for similar strain levels.

iv. Example application: very sensitive permittivity extraction

Since the transmission properties of the gratings reported in [5] is also very sensitive to refractive index of the surrounding media, we analyzed this structure also for permittivity extraction. The schematic of the analyzed grating structure is shown in **Fig. 14a**. The width of the parallel metallic stripes is w, and the period of the stripes is p. The substrates used in this analysis are single-side polished undoped 4'' silicon wafer, double-side polished 2'' sapphire wafer, and single-side polished 1'' β-Ga_2O_3. The semi-insulating Fe-doped CZ-grown (Czochralski) Ga_2O_3 substrate was provided from Northrop Grumman SYNOPTICS. The chosen gratings sizes of each substrate are listed in **Table 1**. The substrate thickness h varies for the different substrates, with nominal thickness listed in **Table 1**. The grating thickness d is set to be 340 nm in the simulation. Full wave electromatic simulations were performed by utilizing the commercial finite element software COMSOL Multiphysics. The simulations were carried out under 2D (x-y) condition. Periodic boundary conditions were applied in the x-direction, and perfectly matched layer conditions were applied in the y-direction. The incident wave with electric field polarized along x direction (TM mode) or z direction (TE mode) propagates normal to the surface. The metallic gold gratings are assumed to have a finite conductivity of $\sigma_m = 4.1 \times 10^7 S/m$.

DISTRIBUTION A: Distribution approved for public release.

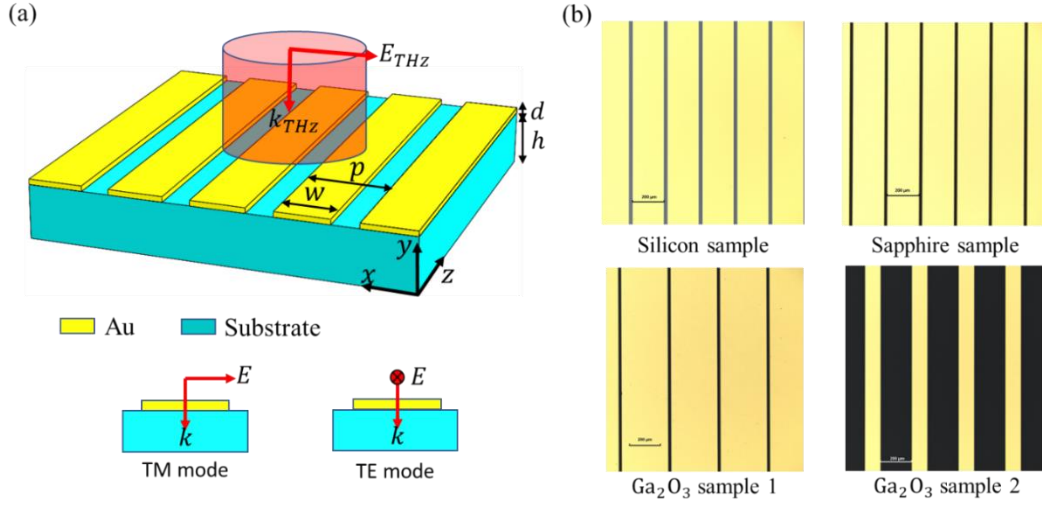

Figure 14. *(a) Schematic of the analyzed grating structure. (b) Optical microscope images of the fabricated metallic gratings on different substrates (the scale bar is 200 μm).*

TABLE I. Summary of the geometrical parameters of the metallic gratings on different substrates.

sample		p (μm)	w (μm)	h (μm)	d (nm)	Mode
Si		220	20	500	348	TM
Sapphire		220	20	430	352	TM
β-Ga_2O_3	Sample 1	320	300	570	358	TM
	Sample 2	300	100	570	358	TM, TE

Metal stacks with target thickness Cr(10 nm)/Au(340 nm) were deposited on the silicon and sapphire substrates using DC sputtering. The same stack was deposited on the β-Ga_2O_3 substrate using e-beam evaporation. Cr was used to improve the adhesion of the metal stack. The metal gratings were patterned using standard photolithography, followed by lift-off. The measured grating thicknesses were 348 nm, 352 nm, and 358 nm for silicon, sapphire, and Ga_2O_3 samples respectively, verified using profilometry and confocal laser scanning microscopy (CLSM).

The transmission spectra of the samples were measured by the frequency-domain polarized terahertz plane wave at normal incidence for frequency ranging from 0.2 THz to 0.6 THz. The frequency scan step size was set to be 0.04 GHz to ensure adequate frequency scan points. The samples, except β-Ga_2O_3 sample 2, were measured with terahertz collimated beam with spot-size bigger than 10 mm in diameter. Only the β-Ga_2O_3 sample 2 was measured with focused terahertz beam with spot size around 10 mm. The air reference measurements were performed for each sample transmission measurement.

DISTRIBUTION A: Distribution approved for public release.

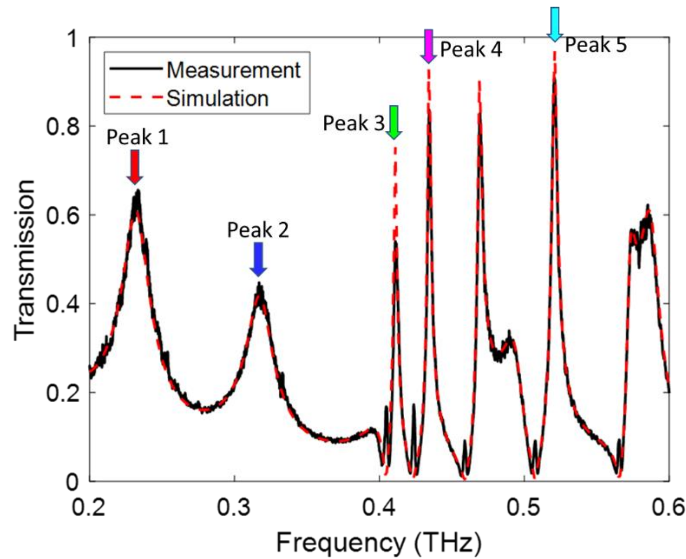

Figure 15. Terahertz transmission spectra of Si sample. Five measured transmission peaks with resonant frequencies 0.2323, 0.3168, 0.4112, 0.4344 and 0.5210 THz are selected for refractive index and thickness fitting.

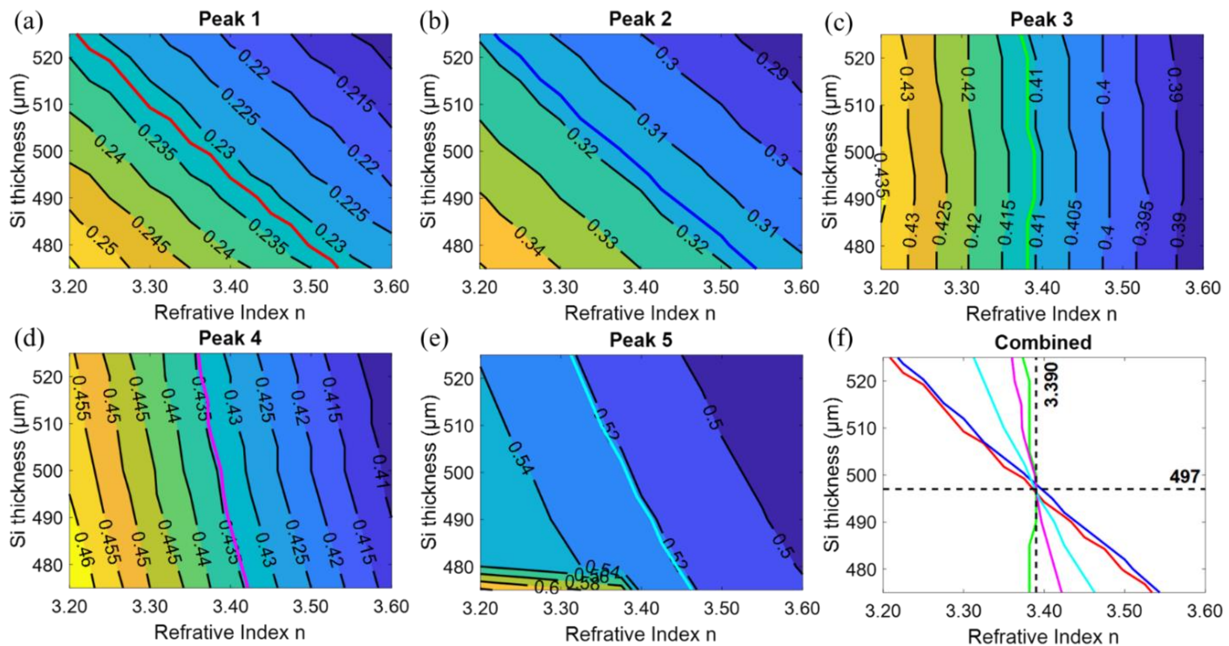

Figure 16. *Thickness and refractive index fitting of Si substrate with selected five resonant frequencies: (a) peak 1 (0.2323 THz), (b) peak 2 (0.3168 THz), (c) peak 3 (0.4112THz), (d) peak 4 (0.4344 THz), (e) peak 5 (0.5210 THz). (f) The combined fitting lines of the selected five resonant frequencies.*

The measured terahertz transmission spectrum of Si sample is shown in **Fig. 15**, displayed by the black curve. Five measured transmission peaks with resonant frequencies 0.2323, 0,3168, 0.4112, 0.4344, and 0.5210 THz are selected for refractive index and thickness of Si substrate fitting. The

DISTRIBUTION A: Distribution approved for public release.

selected resonant frequency values is verified by Lorentzian fitting with 0.1 GHz confidence bound interval width. The thickness of Si was simulated from 475 μm to 525 μm with step size 5 μm. The refractive index value was simulated from 3.20 to 3.60 with step size 0.025. The thickness and refractive index fitting of Si sample of the selected five resonant frequencies are shown in **Fig. 16(a-e)**. **Figure 16(f)** shows the combined fitting lines of the selected five resonant frequencies. As shown in **Fig. 16(f)**, the lines intersect around a point with Si thickness of 497 μm and refractive index 3.390. The simulated transmission spectrum of Si sample is also shown in **Fig. 16**, displayed by the red dashed line. From **Fig. 16**, the resonant peaks of measured transmission spectrum match well with the simulated transmission spectrum for the chosen substrate thickness and refractive index value. The dropped transmission amplitude can be attribute to the imperfect fabrication of lift-off process and metal loss.

The measured terahertz transmission spectrum of sapphire sample is shown in **Fig. 17(c)**, indicated by the black curve. In **Fig. 17(a)**, the selected three resonant peaks with resonant frequencies 0.287, 0.4160, and 0.4495 THz are indicated by the colored arrows. These three resonant frequencies are used for sapphire sample in-plane n(//) and out-of-plane n(⊥) refractive indices fitting. While in **Fig. 17(b)**, three different resonant frequencies 0.2871, 0.4495, and 0.5695 THz are selected for sapphire thickness and in-plane refractive index n(//) fitting.

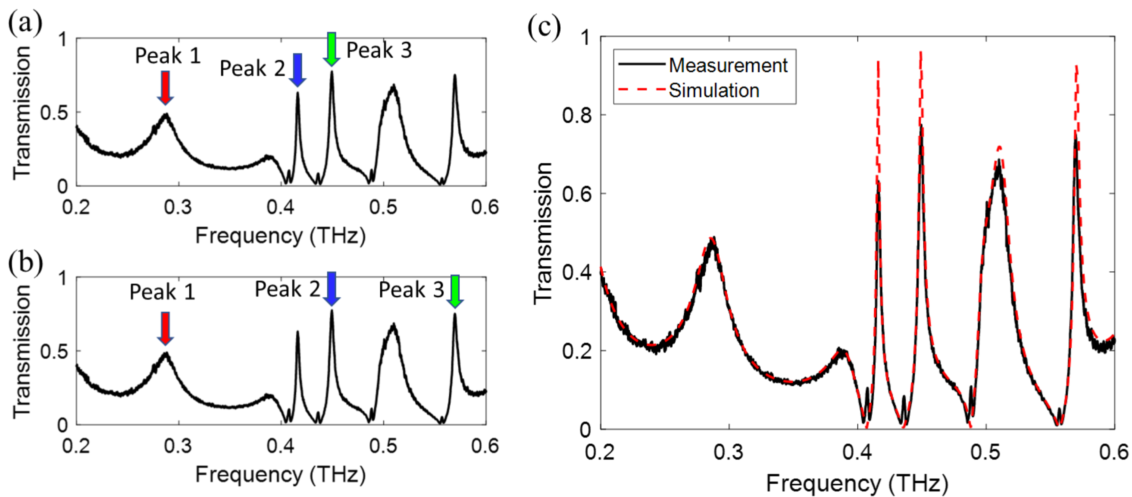

Figure 17. *Terahertz transmission spectra of sapphire sample. (a) The selected three resonant peaks 0.2871, 0.4160, and 0.4495 THz for sapphire sample in-plane and out-of-plane refractive index fitting. (b) The selected four peaks with resonant frequencies 0.2871, 0.4495, 0.5695, and 0.6493 THz for sapphire thickness and in-plane refractive index fitting. (c) The measured and simulated spectra of sapphire sample.*

The in-plane refractive index n(//) and out-of-plane refractive index n(⊥) fitting of sapphire sample of the selected three resonant frequencies 0.287, 0.4160, and 0.4495 THz are shown in **Fig. 18(a-c)**. The simulated in-plane refractive index n(//) varies from 2.90 to 3.40 with step size 0.05, and the out-of-plane refractive index n(⊥) varies from 3.15 to 3.70 with same step size 0.05. The thickness of the sapphire substrate is assumed to be 430 μm in the simulation setting. **Figure 18(d)** shows the combined fitting lines of the selected three resonant frequencies. As shown in Fig. **18(d)**, the lines intersect around a point with the in-plane refractive index 3.130 and out-of-plane refractive index 3.380. **Figures 18(e)** and **18(f)** show the combined fitting lines of the same selected three resonant frequencies with assumed sapphire substrate thickness 420 μm and 440

DISTRIBUTION A: Distribution approved for public release.

μm, respectively. The lines intersect around a point with the in-plane refractive index 3.205 and out-of-plane refractive index 3.380 in **Fig. 18(e)**. While in **Fig. 18(f)**, the intersected point is around the point with in-plane refractive index 3.060 and out-of-plane refractive index 3.380. We can conclude here that the out-of-plane refractive index 3.380 is less independent to the substrate thickness parameter.

So, the thickness parameter of the sapphire sample was mechanically measured and an average thickness value 442 μm was obtained. According to the measured thickness 442 μm, the in-plane refractive index 3.060±0.010 was obtained. The final simulated transmission response of the sapphire sample with thickness 442 μm, in-plane refractive index 3.060, and out-of-plane refractive index 3.380 is shown in **Fig. 17(c)**, displayed by the dashed red line. From **Fig. 17(c)**, the measured transmission response of the sapphire sample matches well with the simulated transmission response of the sapphire sample with the obtained anisotropic refractive indices and thickness parameter.

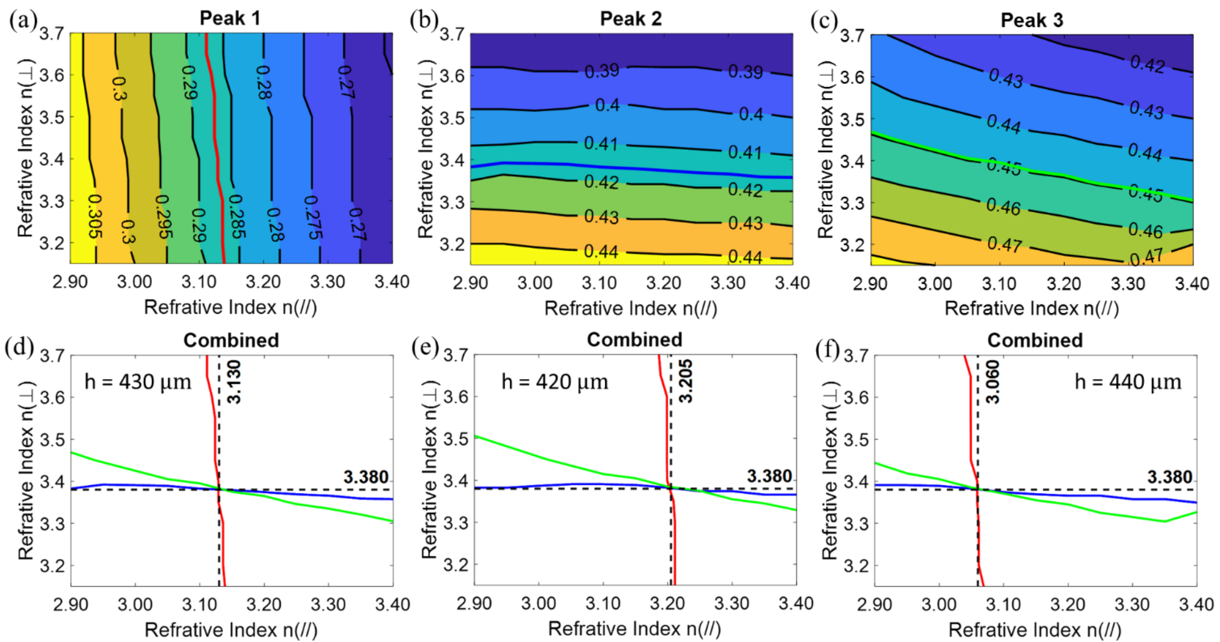

Figure 18. *In-plane n(//) and out-of-plane refractive index n(⊥) fitting of sapphire substrate with the selected three resonant frequencies with thickness h = 430 μm: (a) peak 1 (0.2871 THz), (b) peak 2 (0.4160 THz), (c) peak 3 (0.4495 THz). The combined fitting lines of the selected three resonant frequencies with thickness (d) h = 430 μm, (e) h = 420 μm, and (f) h = 440 μm.*

The anisotropy refractive indices of β-Ga_2O_3 sample were determined by using two different grating sizes, as indicated in **Table 1**. For sample 1, metallic gratings were fabricated along the a*-axis, so the incident electric field is set to be parallel to the c-axis under TM mode. As for sample 2, the metallic grating gold strips were fabricated in the same way that the incident electric field is parallel to the c-axis under TM mode, and parallel to the a*-axis under TE mode. β-Ga_2O_3 sample 1 is used to determine the b-axis and c-axis refractive indices under TM mode, while sample 2 is used to obtain the c-axis refractive index under TM mode, and a*-axis refractive index under TE mode.

DISTRIBUTION A: Distribution approved for public release.

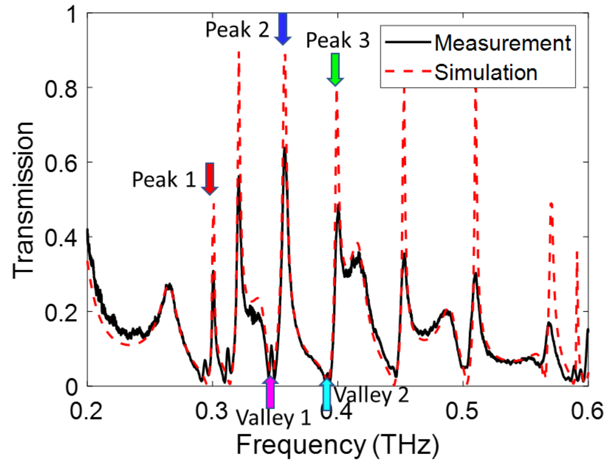

Figure 19. *Terahertz transmission spectrum of β-Ga_2O_3 sample 1. The selected three peaks with resonant frequencies are 0.3005, 0.3576, and 0.4000 THz, and the selected two valleys with frequencies are 0.3472 and 0.3922 THz.*

The measured terahertz transmission spectrum of β-$\mathrm{Ga_2O_3}$ sample 1 is shown in **Fig. 19**. Only peak 1 with resonant frequency 0.3006 THz is selected for crystallographic b-axis refractive index fitting, as indicated by the red color arrow. The effects of β-$\mathrm{Ga_2O_3}$ substrate thickness, a*, c and b axes refractive indices are studied, and the corresponding results are shown in **Fig. 20**. As shown in **Fig. 20(a)**, the resonant peaks shift to lower frequency range as the substrate thickness increases. However, the selected peak 1 resonant frequency maintains almost unchanged. As the incident electric field is parallel to the c axis, perpendicular to the a* axis, so the simulated transmission spectra remain unchanged with varied a*-axis refractive index values, as shown in **Fig. 20(b)**. **Figure 20(c)** displays the simulated transmission spectra with varied **c**-axis refractive index values n(c). With the increasing value of n(c), the resonant peaks shift to lower frequency range. Like **Fig. 20(a)**, the selected peak 1 resonant frequency maintains almost unchanged. Hence, the b-axis refractive index can be obtained by tunning the values of n(b), as indicated by **Fig. 20(d)**, due to the fact the selected peak 1 resonant frequency shifts with different refractive index values of n(b). After running a b-axis refractive index n(b) sweep with fine step size 0.005, the transmission spectrum with obtained n(b) value 3.195 matches the selected peak 1 resonant frequency.

To sum up, we presented a method of refractive index characterization of Si, sapphire, and β-$\mathrm{Ga_2O_3}$ substrates with the assistance of parallel metallic gratings. Frequency-domain polarized terahertz transmission measurement for the terahertz range 0.2 THz to 0.6 THz were performed to obtain the transmission spectra of each sample. The isotropy of silicon, and anisotropy of sapphire and β-$\mathrm{Ga_2O_3}$ substrates were obtained by the fitting the transmission spectrum of each sample through numerical simulations. For the anisotropic β-$\mathrm{Ga_2O_3}$ substrate, its refractive indices along the reciprocal lattice a*-axis direction, and crystallographic axes b and c were extracted to be 3.125, 3.195, and 3.480. This demonstration enables non-destructive characterization for measuring refractive indices of anisotropic low-symmetry materials in the terahertz spectral range, promising a wide range β-$\mathrm{Ga_2O_3}$ opto-electronic device applications.

DISTRIBUTION A: Distribution approved for public release.

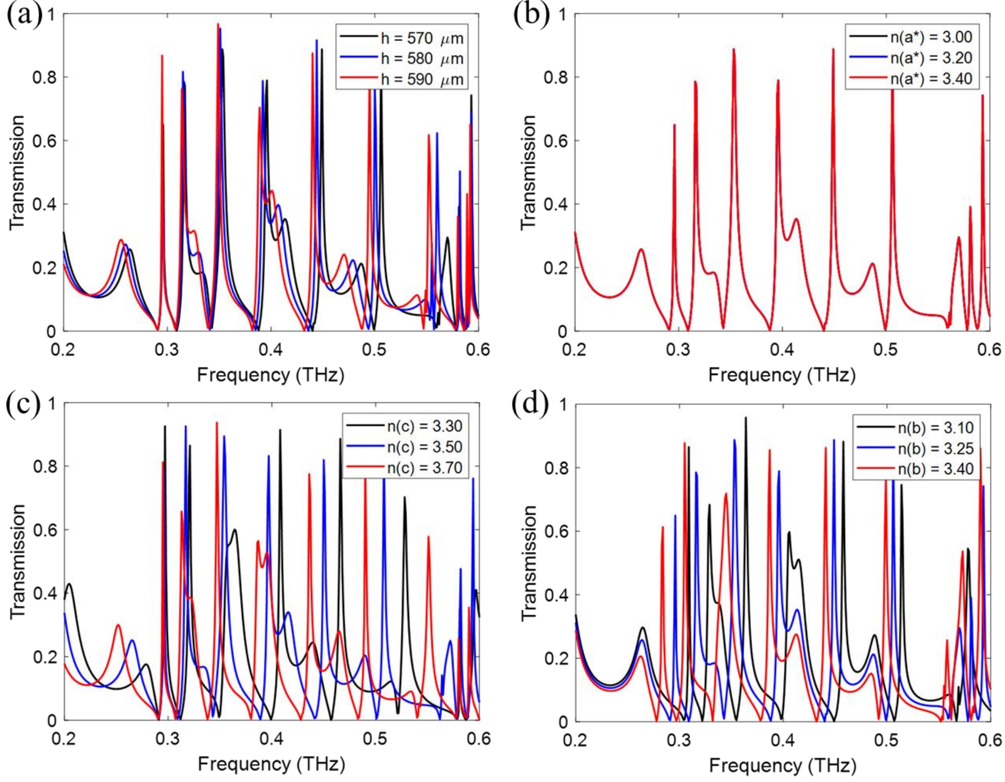

Figure 20. *Simulated terahertz transmission spectra of* β-Ga_2O_3 *sample 1 under TM mode with (a) varied thickness, (b) varied refractive index n(a*), (c) varied refractive index n(c), and (d) varied refractive index n(b).*

Terahertz Metamaterial Modulators Based on III-Nitride Lateral Schottky Diodes

i. Summary

With the advent of 6G communications and the constant quest for more bandwidth in wireless technologies, the use of frequency bands lying in the terahertz spectrum becomes inevitable. Efficient high-speed modulation and demodulation techniques are necessary for the development of future terahertz communication systems. However, the speed of state-of-the-art terahertz modulators is limited to MHz-GHz; therefore, far away from the requirements of practical high-speed communication systems. In this work we demonstrate that lateral Schottky diodes in wide bandgap semiconductors can enable simultaneous high-speed modulation (>100GHz), large modulation depth (>10dB), and low-loss (<3dB) in a metamaterial configuration. These devices are lateral and thus do not require complex semiconductor or electromagnetic design or fabrication. The proposed modulator design approach can therefore unlock the potentials of the terahertz band for future 6G wireless communications.

ii. Motivation

In addition to generation and detection, effective modulation and demodulation technologies are essential for the development of future terahertz communications systems. Similar to what occurs

DISTRIBUTION A: Distribution approved for public release.

in the optical domain, development of high-speed electrically-driven modulators attaining large modulation depths and exhibiting low loss is necessary for the advancement of communications in the terahertz band. Furthermore, devices being capable of efficiently alter the transmission and/or reflection properties of a terahertz beam, although at relatively low speed, could find applications in other important areas such as terahertz imaging. Although in recent years, tremendous achievements have been reported in terahertz modulators, the performance of these in terms of speed is still distant from the state of the art of optical modulators, where speeds in excess of 50 Gbps have been reported. In this context, although recent works have experimentally demonstrated switching speeds on the order of 1 GHz in quasi-optical metamaterial configurations [10], and 14GHz in on-chip waveguide coupled devices [11], these speeds are still relatively low.

To address this issue, metal-semiconductor-metal cavity arrays where operation is based on reverse biasing the Schottky junction formed between top metal strips and a semiconductor buried beneath have been proposed as efficient modulators offering in theory 100% modulation depth, ~10% insertion loss, and picosecond intrinsic switching times [12]. However, the manufacturing of these devices can be challenging due to their vertical nature. It is to note that in this device proposal a relatively thin semiconductor layer, ~2um, is sandwiched vertically between two metal layers, which from a practical perspective can be very difficult to fabricate.

In this work, relying on a similar concept of taking advantage of the intrinsic very high speed of Schottky diodes, we propose a lateral modulator concept capable of attaining similar performance. We explore the different regimes of operation in these devices, as well as discuss the effect of semiconductor choice on its performance. Our results show that wide bandgap materials, such as GaN, could provide advantages in comparison to high mobility semiconductors such as GaAs as a result of a larger breakdown field and relatively good mobility.

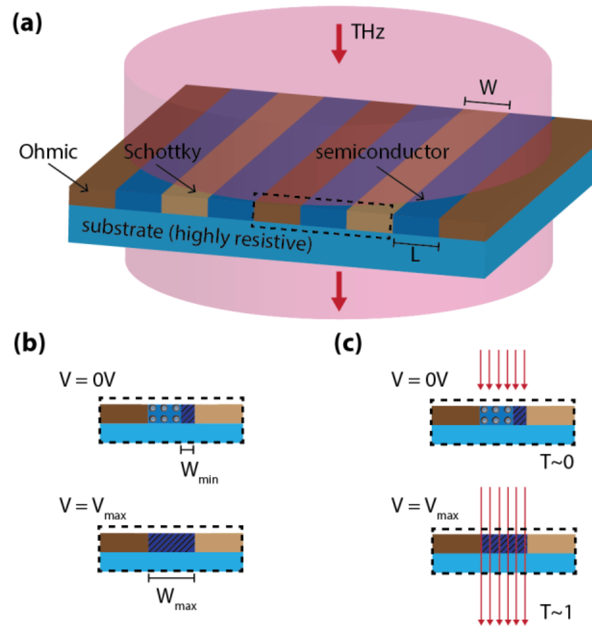

Figure 21. *(a) Schematic of the analyzed device, which consists of an array of lateral Schottky diodes with periodic ohmic and Schottky contacts. A terahertz beam is normally incident to the structure. (b) When*

DISTRIBUTION A: Distribution approved for public release.

applying a voltage (electric field) across the adjacent interdigitated electrodes, the width of the depletion region is controlled. (c) Which in turn controls the transmission of a normally incident THz beam, thus modulates the transmitted intensity.

The analyzed structure consists of an array of lateral Schottky diodes with alternating Schottky and Ohmic contacts, as illustrated in **Fig. 21(a)**. As a reverse voltage (V) is applied, the depletion region width, W, is altered between $W_{max} = L$ and W_{min}, as depicted in **Fig. 21(b)**, which, under full-depletion approximation, are given by:

$$W_{max} = \sqrt{\frac{2\varepsilon(V+V_{bi})}{qN_d}} \text{ and } W_{min} = \sqrt{\frac{2\varepsilon V_{bi}}{qN_d}}. \quad (1)$$

When the device is biased so that $W = W_{min}$, a substantial charge in the semiconductor leads to a low transmission of a normally incident terahertz beam, whereas when the bias is such that $W = W_{max} = L$, then the incident terahertz radiation can funnel through the aperture between adjacent metal contacts and lead to high transmission, as illustrated in **Fig. 21(c)**. The modulation of the depletion width, R, is given by $R = W_{max}/W_{min} = (V/V_{bi}+1)^{1/2}$, and the maximum electric field, which takes place at the semiconductor/Schottky metal interface is given by:

$$E_{max} = \frac{qN_d}{\varepsilon} W_{max} < E_{br}. \quad (2)$$

Therefore, from (1) and (2) it results that for a given reverse bias Nd is bounded by:

$$N_d < \frac{\varepsilon E_{br}}{2q(V+V_{bi})} = N_{d,max}, \quad (3)$$

thus, materials with large E_{br} can provide for larger N_d and thus larger effective conductivity swings, which could translate into a significant modulation of the transmitted THz intensity. The intrinsic cut off frequency (f_0) is:

$$f_0 = \frac{q\mu N_d}{2\pi\varepsilon(R-1)}. \quad (4)$$

Which therefore also benefits from a large N_d, as allowed by a large E_{br}.

From Eqns. (1)-(4), it is possible to generate contour plots of L, E_{max}, V, and f_0 in the (R, σ) plane, where the conductivity (σ) is given by $\sigma = q\mu N_d$. These plots were generated for Si (μ=1,500cm^2/V.s, ε_r=11.7, E_{br}=0.3MV/cm), GaAs (μ=8,500cm^2/V.s, ε_r=12.9, E_{br}=0.4MV/cm), and GaN (μ=1,500cm^2/V.s, ε_r=9.0, E_{br}=3.3MV/cm) and are depicted in **Figs. 22(a)-(c)**. For illustrative and comparative purposes, a uniform value of V_{bi}, $V_{bi} = 0.7$V, was assumed in all three cases. We choose to represent these curves in the (R, σ) plane since in principle, from a modulator perspective, in order to enable large modulation depth, large R and large σ is desirable; therefore, superior designs will be at the upper right corner of this plot. Color-shaded in **Figs. 22(a)-(c)** is the space satisfying L > 100nm, which is chosen as a lithography fabrication constrain, $E_{max} < E_{br}$, and $f_0 >$ 100GHz. It is noticed that GaAs can provide device designs with larger R and σ values than Si because of its larger mobility; whereas GaN can provide for designs operating at similar conductivity levels as GaAs but at larger R levels because of its larger E_{br} (see **Fig. 22(d)**)

DISTRIBUTION A: Distribution approved for public release.

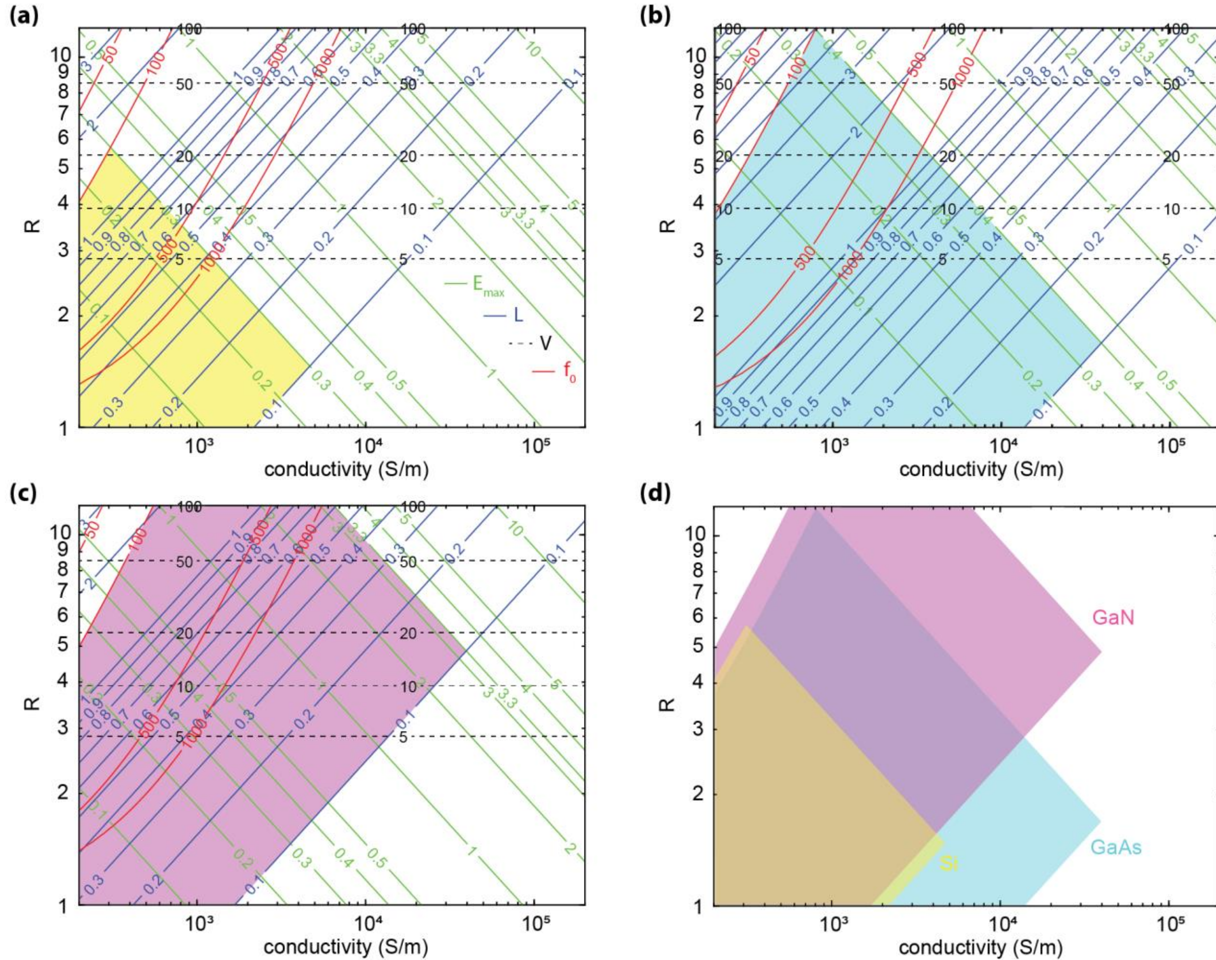

Figure 22. *Design space for (a) Si, (b) GaAs, (c) GaN, (d) comparison (top right corner =preferred region).*

Typical voltage swings for high-speed modulation signals are usually <10V. From this perspective, in **Fig. 23**, we compare device designs in GaAs and GaN under this constrain. In this case, the point leading to superior performance in GaN will be the one corresponding to the intersection of the L=0.1µm curve with the R=3.8 curve, because of the larger conductivity levels attainable in this design. For illustrative purposes we performed full wave electromagnetic simulations in Ansys HFSS for GaN designs with L=0.1, 0.2, 0.3, 0.4, and 0.6um; in these designs in low transmission state a conductivity of 2.3e4, 6.3e3, 2.8e3, 1.6e3, and 6.8e2 S/m over a space region from the ohmic metal to a distance given by L/R from the Schottky metal is assumed. In high transmission state no charge is assumed in the semiconductor (charge is fully depleated). We simulated several designs by varying the width of the metal contacts in the interval 1 to 50µm. Frequency of a normally incident terahertz beam was varied in the 0.1 to 1 THz interval. In this frequency interval, the metal electrodes operate in a broadband extraordinary optical transmission regime [5]. The different points depicted in the modulation depth vs. insertion loss plots in **Figs. 23(b-f)** correspond to different values of W (different colors represent different W) and different frequencies. Because of the larger conductivity level attainable in low transmission state, the L=0.1um designs can produce the larger MD levels. However, these large MD occurs for designs with the largest W's. It is to note that because of the small gap and large metal width, the loss resulting from the final conductivity of the metals in this case leads to a large IL. Looking for

DISTRIBUTION A: Distribution approved for public release.

designs with IL<50% (3dB), the possible modulation depth in this case is ~40-50%. A similar analysis was performed for GaAs, and the results are depicted in **Figs. 23(g)-(l)**, in this case breakdown field in GaAs can limit the possible designs. There is a tradeoff between R and σ and we observe that the best design is when L=0.6um. It is to note that although the maximum attainable modulation depth is smaller than that possible in GaN devices (50% vs. 60%), when comparing the performance of designs attaining <50% loss, the modulation depths are on par.

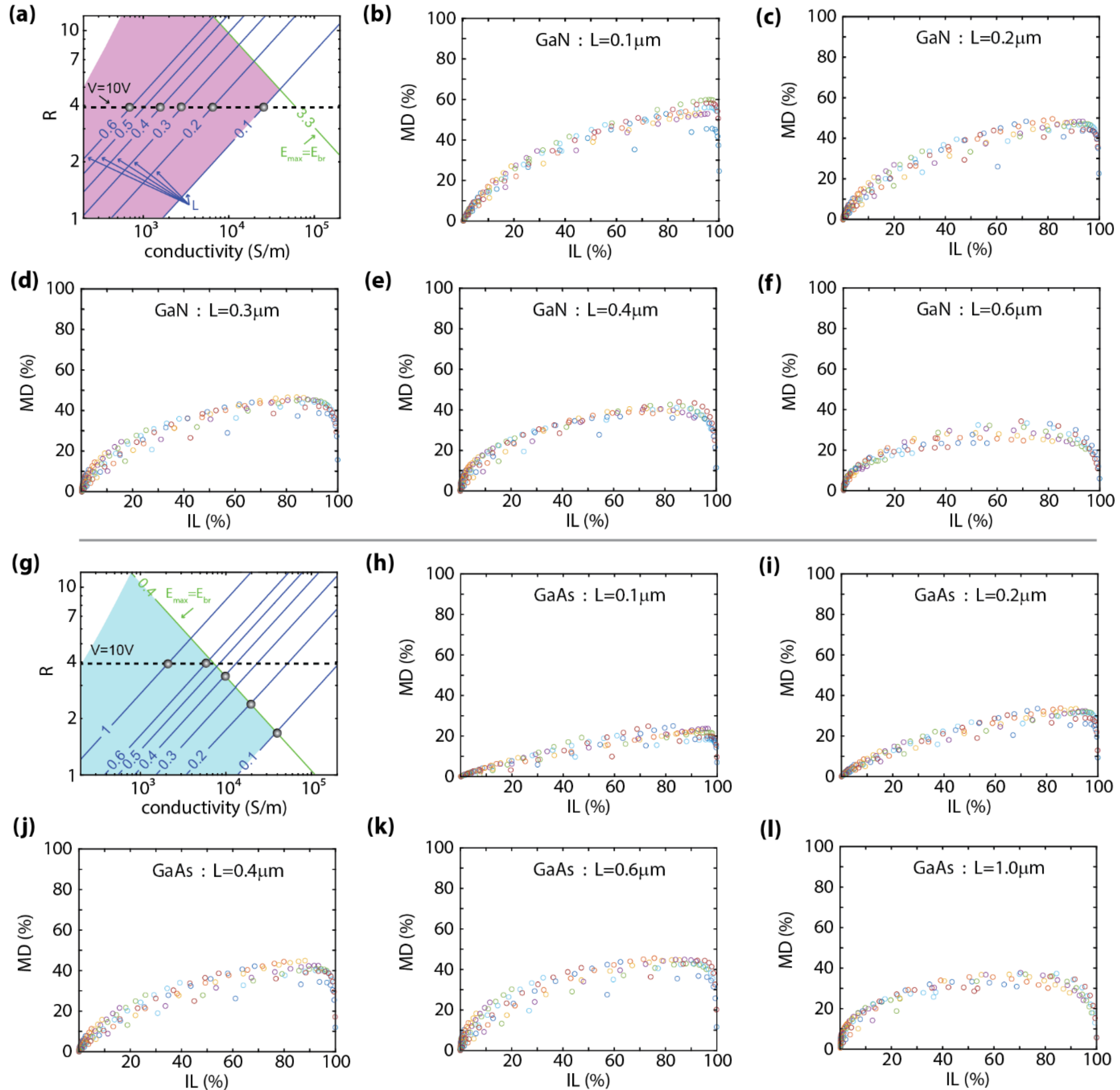

Figure 23. *Modulation performance for (a-f) GaN-based modulators when varying L, and (g-l) GaAs-based modulators, when varying L. Designs are chosen based on <10V operation to enable high speed modulation.*

DISTRIBUTION A: Distribution approved for public release.

Lifting this restriction on voltage swing, we analyzed as well the response of designs in GaN assuming these to be breakdown limited. For this purpose in Fig. **24** we depict designs corresponding to L= 0.1, 0.2, 0.3, 0.4, and 0.6 um, but operating at values of R limited by E_{br}. As a result of this, larger conductivity levels and R are possible than in our analysis in **Fig. 23**. We observe in this case a tradeoff between IL and MD, whereas in designs with the smallest L, large modulation levels are possible only at high loss levels, in designs with largest L, large modulation and low loss is possible. This illustrates that designs operating at larger voltages but with lower N_d could lead to better performance because of a lower possible loss.

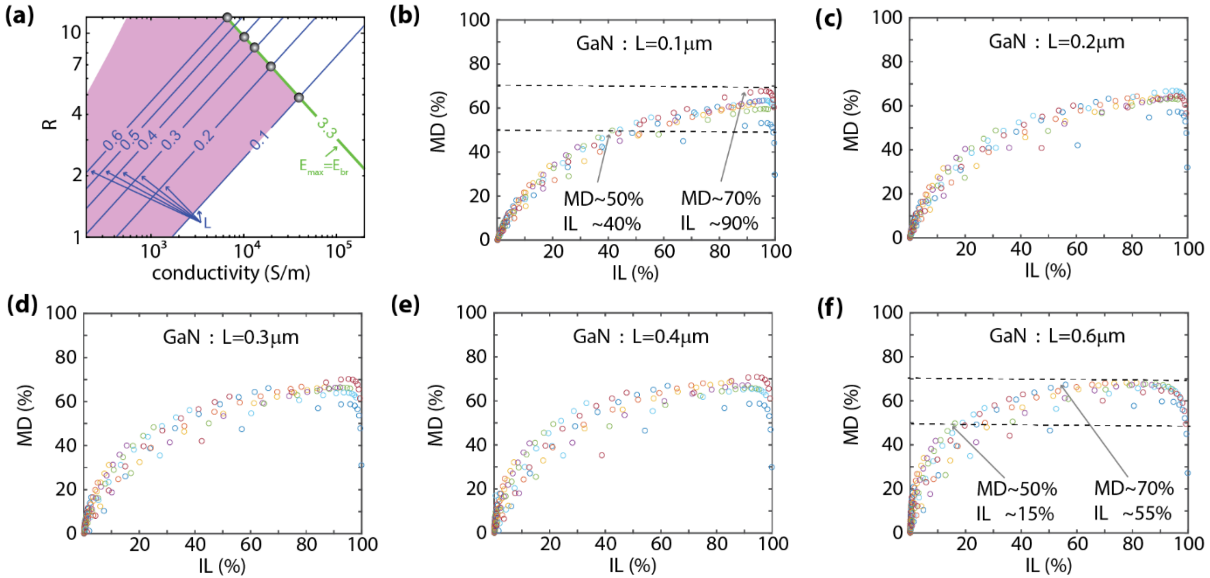

Figure 24. *Modulation performance for (a-f) GaN-based modulators, E_{br} limited, when varying L.*

We now explore these Schottky diode arrays on resonant operation [5]. Comparison of GaN and GaAs devices is depicted in **Fig. 25**. In this case, whereas in GaAs the modulation depth is limited to ~50% (see **Fig. 25(a-c)**), in GaN it is possible to attain >>90% modulation depth (see **Fig. 25 (d-f)**).

Finally, it is to note that an unique property of III-Nitrides is the possibility of enhance mobility / reduce scattering by means of polarization doping. In this regard, utilizing typical mobility values for 2DEGs in AlGaN/GaN QWs, we benchmark in **Fig. 26** how a lateral device consisting of multiple stacked QWs forming a superlattice, with lateral Ohmic and Schottky contacts to 2DEGs will compare with the bulk devices already analyzed. We see in this case that a ~10X larger conductivity is possible vs. GaAs when voltage swing is limited to 10V. Based on this observation, high speed modulation (>100GHz) with large modulation depth (~90%) and low loss (~50%) can be attained in such structures.

DISTRIBUTION A: Distribution approved for public release.

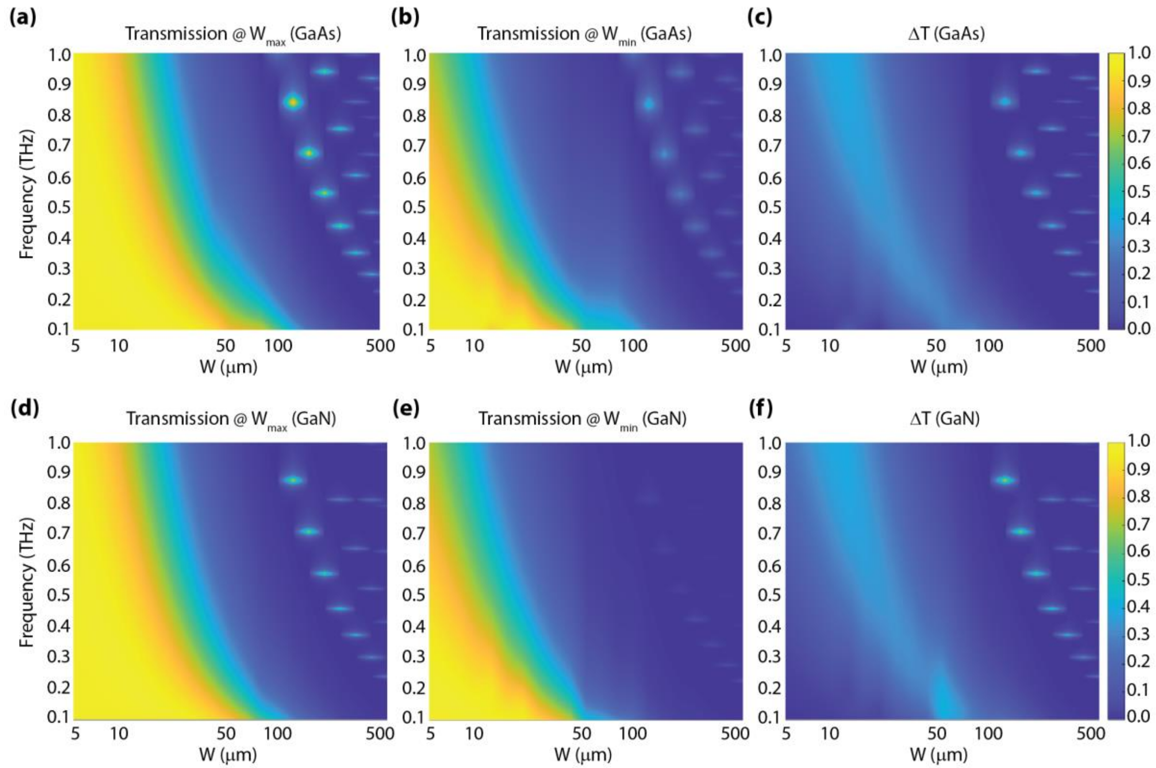

Figure 25. *Comparison of (a-c) GaAs and (d-f) GaN devices under resonant operation.*

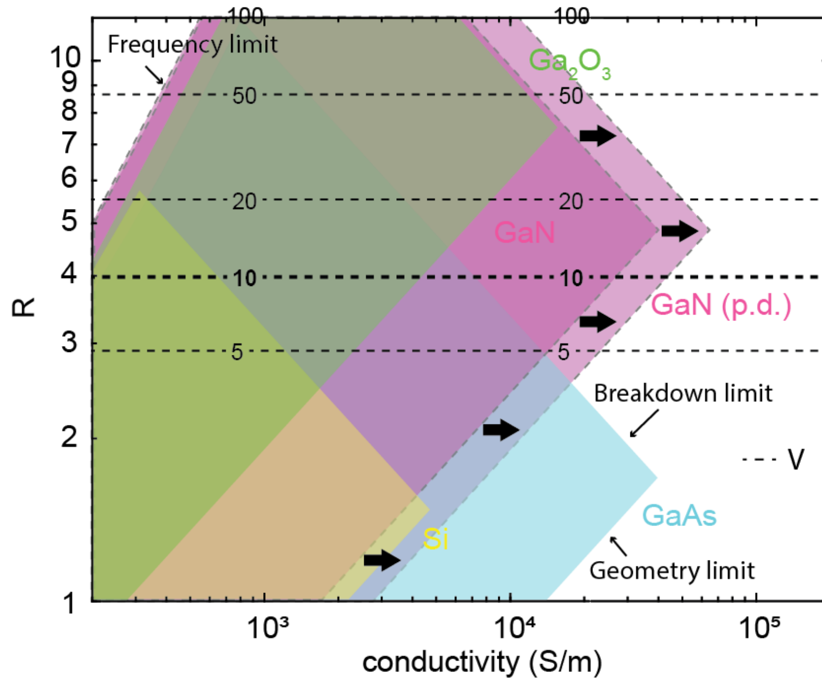

Figure 26. *Polarization doping in superlattices of AlGaN/GaN QWs can further boost the performance of terahertz metamaterial modulators.*

DISTRIBUTION A: Distribution approved for public release.

L. Summary

In this project we explored several new techniques for the terahertz characterization of materials, in particular targeting these towards the study of AlGaN/GaN QWs as well as other wide bandgap materials such as Ga_2O_3. Direct measurements of transmission through these QWs can be employed for chare transport characterization. Through harnessing enhanced light matter interaction in metamaterial structures with subwavelength apertures, we show that it is possible to characterize conductive layers of relatively small conductivity (μS), which is not possible through direct THz transmission measurements. We demonstrate this for the terahertz characterization of the effect of strain on the conductivity of AlGaN/GaN 2DEGs showing through polarization dependent measurements that no significant variations in conductivity occur in such samples through applying strain. We also harness this technique for very sensitive extraction of the out-of-plane component of a material permittivity; based on this we demonstrate that this component can be extracted with error <0.001, which is limited by the scanning step in such measurement due to the narrow linewidth of a Fano resonance arising in the structure whose spectral position depends only in this out-of-plane component and the period of the structure. This technique can find many important applications beyond the ones here shown. We also explore the reciprocal phenomena to show that such structures could be harnessed for promising device applications in the THz band. In this case we show that lateral Schottky diodes based on AlGaN/GaN can enable simultaneous high-speed modulation (>100GHz), large modulation depth (>10dB), and low-loss (<3dB) in a metamaterial configuration. These devices are lateral and thus do not require complex semiconductor or electromagnetic design or fabrication. The proposed modulator design approach can therefore unlock the potentials of the terahertz band for future 6G wireless communications.

M. References

[1] Arezoomandan, S., Condori Quispe, H., Chanana, A., Xu, P., Nahata, A., Jalan, B. and Sensale-Rodriguez, B., 2016. Large nanoscale electronic conductivity in complex oxide heterostructures with ultra high electron density. APL Materials, 4(7), p.076107.

[2] Arezoomandan, S., Prakash, A., Chanana, A., Yue, J., Mao, J., Blair, S., Nahata, A., Jalan, B. and Sensale-Rodriguez, B., 2018. THz characterization and demonstration of visible-transparent/terahertz-functional electromagnetic structures in ultra-conductive La-doped BaSnO 3 Films. Scientific reports, 8(1), pp.3577.

[3] Condori Quispe, H., Islam, S.M., Bader, S., Chanana, A., Lee, K., Chaudhuri, R., Nahata, A., Xing, H.G., Jena, D. and Sensale-Rodriguez, B., 2017. Terahertz spectroscopy of an electron-hole bilayer system in AlN/GaN/AlN quantum wells. Applied Physics Letters, 111(7), p.073102.

[4] Gopalan, P., Knight, S., Chanana, A., Stokey, M., Ranga, P., Scarpulla, M.A., Krishnamoorthy, S., Darakchieva, V., Galazka, Z., Irmscher, K. Fiedler, A., Schubert, M. and Sensale-Rodriguez, B., 2020. The anisotropic quasi-static permittivity of single-crystal β-Ga2O3 measured by terahertz spectroscopy. Applied Physics Letters, 117(25), p.252103.

[5] Gopalan, P., Wang, Y. and Sensale-Rodriguez, B., 2021. Terahertz characterization of two-dimensional low-conductive layers enabled by metal gratings. Scientific Reports, 11(1), pp.2833.

[6] Wang, C., Zhu, H., Wang, S., Chu, D., Liu, K., Jin, L., Li, R., Liu, J., Feng, S., Guo, C. and Zhang, Y., 2020. Effect of Uniaxial Tensile Strains at Different Orientations on the Characteristics

DISTRIBUTION A: Distribution approved for public release.

of AlGaN/GaN High-Electron-Mobility Transistors. IEEE Transactions on Electron Devices, 67(2), pp.449-454.

[7] Dreyer, C.E., Janotti, A. and Van de Walle, C.G., 2013. Effects of strain on the electron effective mass in GaN and AlN. Applied Physics Letters, 102(14), p.142105.

[8] Glavin, N.R., Chabak, K.D., Heller, E.R., Moore, E.A., Prusnick, T.A., Maruyama, B., Walker Jr, D.E., Dorsey, D.L., Paduano, Q. and Snure, M., 2017. Flexible gallium nitride for high-performance, strainable radio-frequency devices. Advanced Materials, 29(47), p.1701838.

[9] Blanton, E.W., Siegel, G., Prusnick, T.A., Glavin, N.R. and Snure, M., 2018. Strain-induced changes in AlGaN/GaN two-dimensional electron gas structures with low surface state densities. Applied Physics Letters, 113(26), p.263503.

[10] Singh, P.K. and Sonkusale, S., 2017. High speed terahertz modulator on the chip based on tunable terahertz slot waveguide. Scientific reports, 7(1), pp.40933.

[11] Zhao, Y., Wang, L., Zhang, Y., Qiao, S., Liang, S., Zhou, T., Zhang, X., Guo, X., Feng, Z., Lan, F. and Chen, Z., 2019. High-speed efficient terahertz modulation based on tunable collective-individual state conversion within an active 3 nm two-dimensional electron gas metasurface. Nano letters, 19(11), pp.7588-7597.

[12] Isić, G., Sinatkas, G., Zografopoulos, D.C., Vasić, B., Ferraro, A., Beccherelli, R., Kriezis, E.E. and Belić, M., 2019. Electrically tunable metal–semiconductor–metal terahertz metasurface modulators. IEEE Journal of Selected Topics in Quantum Electronics, 25(3), pp. 8500108.

DISTRIBUTION A: Distribution approved for public release.